Ionized gas outflow signatures in SDSS-IV MaNGA active galactic nuclei

Dominika Wylezalek [1,2]* Anthony M. Flores,[2] Nadia L. Zakamska [2]
Jenny E. Greene[3] and Rogemar A. Riffel [4,5]

[1]*European Southern Observatory, Karl-Schwarzschildstr. 2, D-85748 Garching bei Muünchen, Germany*
[2]*Department of Physics & Astronomy, Johns Hopkins University, Bloomberg Center, 3400 N. Charles St., Baltimore, MD 21218, USA*
[3]*Department of Astrophysical Sciences, Princeton University, Princeton, NJ 08544, USA*
[4]*Departamento de Física, CCNE, Universidade Federal de Santa Maria, Av. Roraima, 1000, 97105-900 Santa Maria, RS, Brazil*
[5]*Laboratório Interinstitucional de e-Astronomia – LIneA, Rua Gal. José Cristino 77, 20921-400 Rio de Janeiro, RJ, Brazil*

ABSTRACT

The prevalence of outflow and feedback signatures in active galactic nuclei (AGNs is a major unresolved question which large integral field unit (IFU) surveys now allow to address. In this paper, we present a kinematic analysis of the ionized gas in 2778 galaxies at $z \sim 0.05$ observed by Sloan Digital Sky Survey-IV (SDSS-IV) Mapping Nearby Galaxies at Apache Point Observatory (MaNGA). Specifically, we measure the kinematics of the [O III] λ5007 Å emission line in each spatial element and fit multiple Gaussian components to account for possible non-gravitational motions of gas. Comparing the kinematics of the ionized gas between 308 MaNGA-selected AGNs that have been previously identified through emission-line diagnostics and sources not classified as AGN, we find that while 25 per cent of MaNGA-selected AGN show [O III] components with emission-line widths of >500 km s^{-1} in more than 10 per cent of their spaxels, only 7 per cent of MaNGA non-AGNs show a similar signature. Even the AGNs that do not show nuclear AGN photoionization signatures and that were only identified as AGN based on their larger scale photoionization signatures show similar kinematic characteristics. In addition to obscuration, another possibility is that outflow and mechanical feedback signatures are longer lived than the AGN itself. Our measurements demonstrate that high velocity gas is more prevalent in AGN compared to non-AGN and that outflow and feedback signatures in low-luminosity, low-redshift AGN may so far have been underestimated. We show that higher luminosity MaNGA-selected AGNs are able to drive larger scale outflows than lower luminosity AGN. But estimates of the kinetic coupling efficiencies are $\ll 1$ per cent and suggest that the feedback signatures probed in this paper are unlikely to have a significant impact on the AGN host galaxies. However, continuous energy injection may still heat a fraction of the cool gas and delay or suppress star formation in individual galaxies even when the AGN is weak.

Key words: techniques: imaging spectroscopy – techniques: spectroscopic – galaxies: active.

1 INTRODUCTION

The energy output of actively accreting supermassive black holes [active galactic nuclei (AGNs)] has become a critical ingredient in modern galaxy formation theories. Powerful AGN (quasars, L_{bol} $> 10^{45}$ erg s^{-1}) can heat and photoionize gas tens of kiloparsecs away, and even well into the circumgalactic medium (Johnson, Chen & Mulchaey 2015; Rudie, Newman & Murphy 2017) in a process known as radiative feedback. Furthermore, radiatively driven nuclear winds (Murray et al. 1995) or jets can launch galaxy-

wide outflows. Such mechanical feedback processes can aide in establishing the black hole versus bulge correlations, can effectively quench star formation activity, and – most importantly – set the upper limit to the masses of galaxies (e.g. Ferrarese & Merritt 2000; Croton et al. 2006; Fabian 2012; Kormendy & Ho 2013). However, constraining the power and reach of such feedback processes exerted by black holes on to their hosts remains a major unresolved issue in modern extragalactic astrophysics.

The critical role of quasars in galaxy formation was hypothesized two decades ago (Silk & Rees 1998), yet this paradigm only recently obtained observational support, much of it on the basis of IFU observations (Rupke & Veilleux 2011; Liu et al. 2013; Harrison et al. 2014; Carniani et al. 2015). There is increasing evidence that

* E-mail: dwylezal@eso.org

in powerful AGN the main interaction with the gas is through winds, which are inhomogeneous, complex multiphase phenomena, with different gas phases observable in different spectral domains (Heckman, Armus & Miley 1990; Veilleux, Cecil & Bland-Hawthorn 2005). Most of our current knowledge about AGN-driven outflows comes from mapping the kinematics of the warm ionized gas phase via optical emission lines such as [O III] 5007 Å. The signature of galaxy-wide winds is that of gas on galactic scales moves with velocities inconsistent with a dynamical equilibrium with the host galaxy or disc rotation (Liu et al. 2013; Rupke & Veilleux 2013b; Wylezalek et al. 2016, 2018).

Integral field unit (IFU) surveys now offer new possibilities in characterizing outflow signatures for statistically significant samples. The Sloan Digital Sky Survey-IV (SDSS-IV; Blanton et al. 2017) survey Mapping Nearby Galaxies at APO (MaNGA; Bundy et al. 2015; Drory et al. 2015; Law et al. 2015; Yan et al. 2016a,b; Wake et al. 2017) is a new optical fibre-bundle IFU survey and will obtain IFU observations of 10 000 galaxies at $z \lesssim 0.1$ over the next few years, allowing an extensive investigation of the spatial dimension of galaxy evolution. The goals of the survey are to improve the understanding on the processes involved in galaxy formation and evolution over time.

Mapping Nearby Galaxies at Apache Point Observatory (MaNGA) also allows to take full advantage of the spatial dimension of AGN ionization signatures (Penny et al. 2017; Rembold et al. 2017; Sanchez et al. 2017; Wylezalek et al. 2017, 2018). Wylezalek et al. (2018) have recently developed spatially resolved techniques tailored to the MaNGA data for identifying signatures of AGN. Out of 2778 galaxies in the parent sample, they identify 303 AGN candidates which show signatures of gas ionized by relatively hard radiation fields inconsistent with star formation. While the authors show that ~10 per cent of low-redshift galaxies currently host low- to intermediate-luminosity AGN based on photoionization diagnostics, it remains unclear if and to what extent these AGN impact the gas kinematics through AGN-driven winds. Additionally, Wylezalek et al. (2018) show that about a third to half of the MaNGA-selected AGN candidates would not have been selected based on the SDSS-III single-fibre observations since AGN ionization signatures are only prevalent beyond the 3 arcsec coverage of the single-fibre spectra. Reasons for such signatures can be manyfold (heavy circumnuclear obscuration, off-nuclear AGN, dominant nuclear SF signatures, relic AGN) and are currently under investigation.

A particularly intriguing possibility is that some of the AGN candidates are relic AGN. In such objects the nuclear activity subsided some time ago, but the photoionization signatures at large distances persist for 10^4–10^5 yr due to light-travel delays and radiative time-scales of emitting gas (Lintott et al. 2009; Schawinski et al. 2015a; Sartori et al. 2016; Keel et al. 2017). In relic AGN, kinematic signatures of previous AGN activity may be longer lived than nuclear photoionization signatures (Ishibashi & Fabian 2015). Investigating the ionized gas kinematics in currently active AGN with nuclear AGN signatures and relic AGN candidates is therefore of great interest with respect to outflow time-scales and outflow propagation.

In this paper, we investigate the prevalence of ionized gas outflow signatures in MaNGA-selected AGN. This work focuses on a detailed kinematic analysis of the [O III] λ4959,5007 Å doublet. We first develop a spaxel-based fitting algorithm allowing broad secondary components in the emission-line profile to be accounted for. Our goal is to improve on the kinematic measurements previously made by the survey pipeline and use them in conjunction with a sample of independently identified AGN candidates from Wylezalek et al. (2018).

The paper is organized as follows: Section 2 introduces the MaNGA survey and structure of the available data. Section 3 presents the spectroscopic fitting procedure, while Section 4 presents the kinematic analysis. In Section 5, we discuss the identification of ionized gas outflow signatures and their prevalence in MaNGA-selected AGN and non-AGN. In Section 6, we present our conclusions. To statistically compare distributions, we use the two-sample Kolmogorov–Smirnov test and report p, the probability of the null hypothesis that the two samples are drawn from the same distribution. Low p values ($p < 0.01$) mean that the two samples are statistically different. Throughout the paper we use $H_0 = 72$ km s^{-1} Mpc^{-1} and $\Omega_m = 0.3$, $\Omega_\Lambda = 0.7$.

2 DATA

2.1 The MaNGA survey and data products

MaNGA is a spectroscopic survey as part of the SDSS-IV. MaNGA is a two-dimensional spectroscopic survey that uses IFU observations to take multiple spectral observations of each galaxy in the 3600–10 000 Å range using the BOSS Spectrograph (Gunn et al. 2006; Smee et al. 2013) at $R \sim 2000$. Fibres are arranged into hexagonal groups, with bundle sizes ranging from 19–127 fibres, depending on the apparent size of the target galaxy (which corresponds to diameters ranging between 12 and 32 arcsec), leading to an average footprint of 400–500 arcsec^2 per IFU. The fibres have a size of 2 arcsec aperture (2.5 arcsec separation between fibre centres), which at $z \sim 0.05$ corresponds to ~2 kpc, although with dithering the effective sampling improves to 1.4 arcsec. The current data release DR14 (Abolfathi et al. 2018) contains 2778 galaxies at $0.01 < z < 0.15$ with a mean $z \sim 0.05$. Over the next three years, MaNGA will have obtained observations of ~10 000 galaxies at $z \lesssim 0.15$ and with stellar masses > 10^9 M$_\odot$.

The MaNGA Data Reduction Pipeline (DRP) produces sky-subtracted spectrophotometrically calibrated spectra and rectified three-dimensional data cubes that combine individual dithered observations (for details on MaNGA data reduction see Law et al. 2016) with a spatial pixel scale of 0.5 arcsec pixel^{-1}. The median spatial resolution of the MaNGA data is 2.54 arcsec full width half-maximum (FWHM) while the median spectral resolution is ~72 km s^{-1} (Law et al. 2016). The MaNGA Data Analysis Pipeline (DAP; Yan et al. 2016b; Westfall) is a project-led software package used to analyse the data products provided by the MaNGA DRP, providing the collaboration and public with survey-level quantities, such as stellar-population parameters, kinematics, and emission-line properties for 21 different emission lines. To make these calculations, the DAP first fits the stellar continuum using the Penalized Pixel-Fitting method (pPXF; Cappellari & Emsellem 2004; Cappellari 2017) and then subtracts the best-fitting stellar continuum from the observed data before fitting single Gaussians to the emission lines, allowing for additional subtraction of a non-zero baseline. The final fitting model, emission-line fit, and baseline fit are all available via the 'MODEL,' 'EMLINE,' and 'EMLINE_BASE' extensions, respectively, in the DAP logcube files.

2.2 Samples

The work in this paper is based on the Data Release 14 (DR14) which consists of data cubes for 2778 galaxies for 2727 unique objects.

Table 1. Mean and 75th percentile [O III] velocity width measurements $\langle W_{80} \rangle$ and $W_{80, 75th}$ of all MaNGA galaxies analysed in this work. The column f_{spx} reports the fraction of spaxels with high S/N [O III] emission-line measurements with S/N > 10. The last two columns report whether the source is identified as a MaNGA-selected AGN (flag1 = 1), a MaNGA non-AGN (flag1 = 0). If identified as a MaNGA-selected AGN, the flag2 column denotes whether this source is an SF-AGN (flag2 = 2), LINER-AGN (flag2 = 3) or Seyfert-AGN (flag2 = 4, see Section 2.2 for more details on the subsample definitions).

MaNGA ID	RA (deg)	Dec. (deg)	z	$\langle W_{80} \rangle$ (km s^{-1})	$W_{80, 75th}$ (km s^{-1})	f_{spx}	flag1	flag2
1-109056	39.4465871047	0.405085157798	0.0473019	249	278	0.34	1	4
1-109073	42.1567757009	− 0.554292603774	0.0435882	197	203	0.54	0	0
1-109081	41.694639931	− 0.728826852116	0.0438592	""	""	0.0	0	0
1-109112	41.3609282489	0.91013274057	0.0249702	""	""	0.0	0	0
1-109167	42.2169259383	− 0.524053160567	0.0246344	312	302	0.11	0	0
1-109308	49.9495621925	− 0.22114540619	0.131681	""	""	0.0	1	2
1-109356	50.0738407878	0.523632230733	0.0241782	213	216	0.62	0	0
1-109378	51.1699181501	− 0.681472614144	0.0391104	366	418	0.11	0	0
1-109394	50.179936141	− 1.0022917898	0.0361073	345	364	0.32	0	0
1-109428	54.602285942	− 0.0185818400418	0.0476594	""	""	0.0	0	0

Note. Only a portion of this table is shown here to demonstrate its form and content. A machine-readable version of the full table is available as online material.

The aim of this work is to compare the kinematic characteristics of the [O III] emission line for MaNGA-selected AGN and non-AGN in the MaNGA sample. In optical surveys, emission-line flux ratios and diagnostic diagrams are the most common way to identify AGN (Baldwin, Phillips & Terlevich 1981; Osterbrock 1989; Kauffmann et al. 2003; Zakamska et al. 2003; Kewley et al. 2006; Reyes et al. 2008; Yuan, Strauss & Zakamska 2016). But a major caveat of large optical spectroscopic surveys such as the Sloan Digital Sky Survey (prior to MaNGA) is the small size of the optical fibres which, at 3 arcsec diameter (in the case of SDSS-I to SDSS-III surveys), only cover a fraction of the footprint of a galaxy and are only sensitive to processes close to the Galactic Centre.

Wylezalek et al. (2018) recently developed spatially resolved techniques for identifying signatures of AGN tailored to MaNGA IFU data identifying 303 AGN candidates. A minor update to the selection code[1] has increased the sample to 308 sources which we adopt as the 'AGN' sample in this work (see Table 1). We furthermore refer to remaining MaNGA galaxies as 'non-AGN'. While LINER-like ('low ionization nuclear emission-line region') galaxies can be associated with a number of ionization mechanisms such as weakly ionizing AGN (Heckman 1980), shock ionization (either related to star-forming processes in inactive galaxies or AGN activity), or photoionization through hot evolved stars, the algorithm developed by Wylezalek et al. (2018) was tailored to select the most likely AGN among LINER-like galaxies. This has been achieved using combination of spatially resolved line diagnostic diagrams, assessing the significance of the deviation from the star formation locus in line diagnostic diagrams and applying additional cuts on H α surface brightness and H α equivalent width.

Some of the AGN candidates selected by Wylezalek et al. (2018) would not have been identified based on the single-fibre nuclear spectra alone. This is either because the AGN is hidden behind large columns of dust in the Galactic Centre, because the AGN has recently turned off and relic AGN signatures are only visible at larger distances, because the AGN is offset after a recent galaxy merger, or because a circumnuclear starburst overwhelms nuclear AGN signatures (Wylezalek et al. 2018). Based on the MaNGA measurements in the inner 3 arcsec (similar to the single fibre

classifications of SDSS I-III), 109 out of the 308 MaNGA-selected AGN would be classified as star-forming (SF) galaxies, 84 sources would be classified as 'Seyfert' galaxies, i.e. AGN, and 91 sources would be classified as LINER-like galaxies. In the remaining part of the paper, we refer to these subsamples as Seyfert-AGN (84 sources), SF-AGN (109 sources), and LINER-AGN (91 sources). The 24 remaining galaxies could not be classified based on their central emission-line signatures due to one or more needed emission lines not fulfilling the required S/N criteria (see Wylezalek et al. 2018, for the details of the selection). In the remaining part of the paper, we do not include these galaxies when assessing the differences between the individual 'types' of AGN.

We note that this AGN selection is different to the ones used in Rembold et al. (2017) or Sanchez et al. (2017) who both present results on AGN in MaNGA. The main difference in the sample selection is that both of these works only use the photoionization signatures in the central region of the galaxies to classify a galaxy as an AGN candidate. Rembold et al. (2017) use the SDSS-III spectroscopic data from DR12 based on the 3 arcsec single-fibre measurements whereas Sanchez et al. (2017) use the MaNGA spectroscopic information in the central 3 arcsec × 3 arcsec region analysed and measured with the PIPE3D pipeline (Sánchez et al. 2016). Their AGN samples contain 62 and 98 AGN candidates. The differences in the sample selection lie in the exact choice of diagnostic diagrams and equivalent width cuts. For example, while Rembold et al. (2017) employ a cut of 3 Å on the equivalent width of H α, Sanchez et al. (2017) use a more relaxed criterion of only 1.5 Å. These differences lead to different and less/more sources being selected as AGN candidates. The overlap between the Wylezalek et al. (2018) and Rembold et al. (2017) samples is 37 sources, the overlap between the Wylezalek et al. (2018) and Sanchez et al. (2017) samples is 44 sources, and the overlap between the Rembold et al. (2017) and Sanchez et al. (2017) samples is 37 sources. In Comerford et al. (2020), we explore the overlap between optical and radio selected AGN in MaNGA and are furthermore exploring the implications for BPT and H α selection of AGNs in a subsequent paper (Negus et al., in preparation).

3 METHODS

3.1 Spectral fitting

In this paper, all kinematic calculations are made based on fits of the emission lines of the [O III] doublet line at 5008/4960Å. All

---

[1]This minor update regards the inclusion of a few 'borderline' objects related to the precision with which d_{BPT}, the distance between Seyfert/LINER-classified spaxels in the BPT diagram and the star formation demarcation line, is measured (see Wylezalek et al. 2018 for more details).

SDSS data, including MaNGA, are stored at vacuum wavelengths (Morton 1991) but we use air wavelengths to identify emission lines following the long-standing convention. In AGN, a large fraction of the [O III] emission originates in the narrow-line regions surrounding the AGN (e.g. Kewley et al. 2006; Liu et al. 2013). Being a forbidden line, it can therefore trace the low-density AGN-ionized gas even out to galaxy-wide scales of several kiloparsecs (Liu et al. 2013). [O III] is easily observable from the ground for low to intermediate redshift AGN and it is widely used as a gas (outflow) tracer in low- and intermediate-redshift AGN (Crenshaw et al. 2010, 2015; Lena et al. 2015; Fischer et al. 2017; Rupke, Gültekin & Veilleux 2017), making our measurements easily comparable with other works.

We develop a customized fitting procedure to model the [O III] doublet and potential secondary and/or broad components in the line. We first extract the spectra for each spaxel from the DAP Logcube files using the 'FLUX' extension, providing the flux density in units of 10^{-17} erg s^{-1} cm^{-2} Å^{-1} spaxel^{-1} and then subtract the modelled stellar continuum (see Section 2.2) using the other Logcube extensions. We then also measure the flux-level blue- and red-ward of the Hβ + [O III] line complex to subtract any additional continuum contributions using a linear function of wavelength that might not have been accounted for. We further adopt the spectroscopic redshifts from the NASA Sloan Atlas (NSA) catalogues that are based on the single-fibre measurements to correct the spectra to the rest frame of the galaxy.

The MaNGA Data Analysis pipeline performs single Gaussian fitting on a number of selected, bright emission lines in all spaxels. However, a single Gaussian is often insufficient for describing the profile of the [O III] line, and in particular such a fit would fail to capture a secondary broad component characteristic of outflowing gas. To evaluate the prevalence of additional kinematic components in MaNGA-selected AGN, we therefore allow multiple Gaussian components to be fit to the emission lines. In the fitting process, we fit the two transitions of the [O III] doublet simultaneously and assume they share the same kinematics. We furthermore fix the ratio between the amplitude of the 5008 Å peak and the 4960 Å peak to its quantum value of 2.98. The fitting procedure uses least-squares regression to return best-fitting parameters for the single-Gaussian and double-Gaussian models. We evaluate the goodness of the fit based on its χ^2 value and use the fit that both minimizes the number of Gaussian components and its χ^2. While in the two-dimensional maps, we show all spaxels where the signal-to-noise ratio of the [O III] emission lines S/N > 3, we only use spaxels with S/N > 10 in the subsequent analysis part of this paper. In Fig. 1, we show an example fit to a spaxel in the MaNGA galaxy 8715-3702 where our multiple component Gaussian fitting describes the line profile more accurately than the standard single Gaussian fit.

3.2 Non-parametric values

When spectra can be well described based solely by single Gaussian fits, then the calculation of best-fitting parameters such as velocity dispersion σ, FWHM, amplitude are sufficient to describe the kinematic properties of the emission line in that spaxel. This is not the case when multiple Gaussians are used to describe the line profile. Because the sum of multiple Gaussians is used in some spaxels, we calculate non-parametric values based on percentages of the total integrated flux and follow the measurement strategy presented in Zakamska & Greene (2014) and Liu et al. (2013) (see also Whittle 1985) to determine amplitudes, centroid velocities and
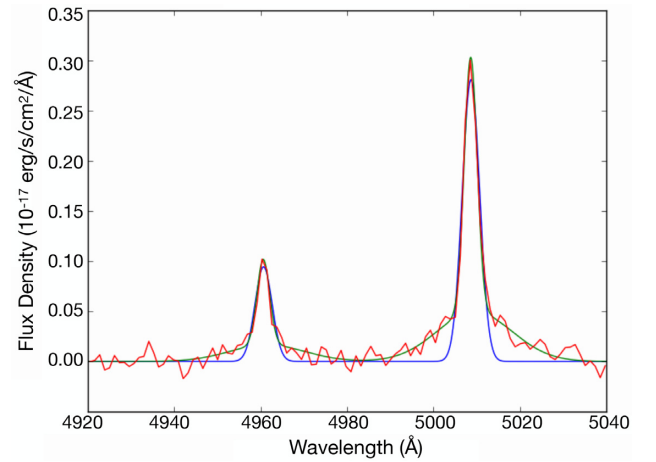

Figure 1. An example fit for a spaxel in MaNGA galaxy 8715-3702. The spectrum after subtraction of the stellar continuum is shown in red, the single Gaussian fit is shown in blue, and the multi-Gaussian fit is shown in green. While the single Gaussian fit (blue) misses the broad wings in the line profile, the multi-Gaussian fit provides a much more accurate description of the line profile and its associated kinematic properties.

emission-line widths. Such non-parametric measurements do not strongly depend on a specific fitting procedure.

The cumulative flux as a function of velocity is

$$\Phi(v) = \int_{-\infty}^{v} F_v(v') \mathrm{d}v' \qquad (1)$$

and the total line flux is given by $\Phi(\infty)$. In practice, we use the interval [−2000, 2000] km s^{-1} in the rest frame of the galaxy for the integration. For each spaxel, we compute the line-of-sight velocity v_{med} where $\Phi(v_{\mathrm{med}}) = 0.5 \cdot \Phi(\infty)$, i.e. this is the velocity that bisects the total area underneath the emission-line profile. Because the fitting is performed in the rest frame of the galaxy as determined by its stellar component, v_{med} is measured relative to the rest frame. We use the W_{80} parameter to parametrize the velocity width of the line. W_{80} refers to the velocity width that encloses 80 per cent of the total flux. For a purely Gaussian profile, W_{80} is close to the FWHM but the non-parametric velocity width measurements are more sensitive to the weak broad bases of non-Gaussian emission-line profiles (Liu et al. 2013). We first determine v_{90} such that $\Phi(v_{90}) = 0.9 \cdot \Phi(\infty)$ and v_{10} such that $\Phi(v_{10}) = 0.1 \cdot \Phi(\infty)$ and then calculate W_{80} using $W_{80} = v_{90} - v_{10}$.

3.3 Kinematic and division maps

Having performed the fitting and analysis procedure described in Sections 3.1 and 3.2 in all spaxels of MaNGA-selected AGN candidates, we create two-dimensional maps for the following quantities:

(i) The total flux measured for [O III]5008 Å.
(ii) The non-parametric line-of-sight velocity $v_{\mathrm{med.}}$
(iii) The non-parametric velocity width $W_{80}.$
(iv) The number of Gaussians used for each fit determined based on the χ^2 analysis.
(v) The reduced χ^2 statistic of the best fit in each spaxel.

The MaNGA survey team has already made velocity dispersion calculations σ_{DAP} based on a single Gaussian fits to the [O III] emission lines in each spaxel. In order to assess how well these
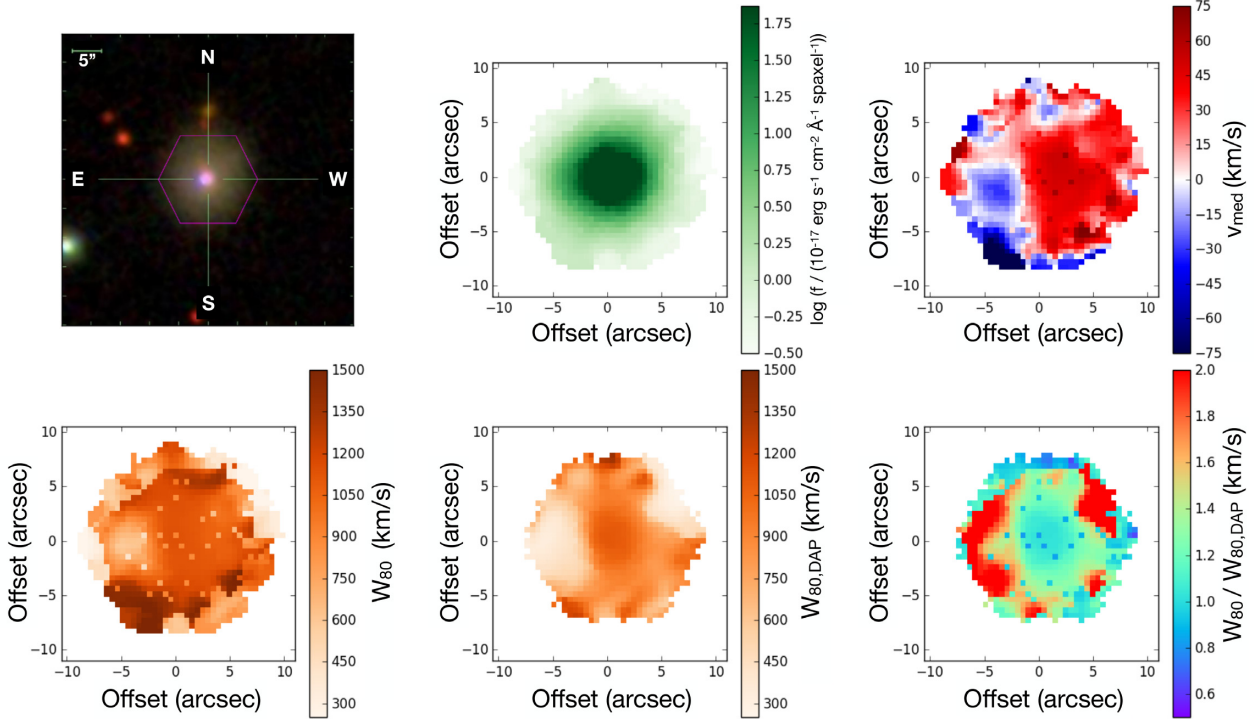
Figure 2. Example maps for MaNGA galaxy 8715-3702. We show the SDSS composite *gri* optical (top left), the [O III] flux density (Logarithmic, top centre), the median velocity v_{med} (top right), the multi-Gaussian-based W_{80} measurements (lower left), the reference, single-Gaussian-based $W_{80,\,DAP}$ values based on the MaNGA Data Analysis Pipeline fits (lower centre), and the divisional values $\frac{W_{80}}{W_{80,\,DAP}}$ (lower right). All images and maps are orientated north-up, east-left.

single Gaussian fits describe the lines and how the velocity dispersion based on the single Gaussian fits compares to the dispersion derived in this work, we generate 'division maps' for every galaxy in the survey. The 'division maps' report the fractional difference in velocity dispersion when comparing the single Gaussian fits to our measurements. To achieve a fair comparison, we first compute the non-parametric velocity dispersion W_{80} for the single Gaussian fits from the MaNGA DAP. As mentioned above, for a purely Gaussian profile, W_{80} is closely related to the FWHM and therefore to its velocity dispersion, such that:

$$W_{80,DAP} = 1.088 \times FWHM_{DAP} = 1.088 \times 2.35\sigma_{DAP} = 2.56 \times \sigma_{DAP}.$$
(2)

We then divide the W_{80} value derived from our multi-Gaussian customized fitting procedure described above by the corresponding DAP single-Gaussian based $W_{80,DAP}$ value in each spaxel. This results in a two-dimensional map for each galaxy reporting divisional values (i.e. fractional differences in velocity line width measurements) across the galaxy. Values in this map ∼1 identify the spaxels where our fits, either single or double, are similar to the DAP ones, while higher values flag the spaxels where the double Gaussian fit captured a secondary component in the emission line missed by the DAP. In the subsequent analysis, we utilize these maps to assess the prevalence of additional kinematic ionized gas components in MaNGA galaxies and MaNGA-selected AGN.

In Figs 2, 3, and 4, we show three examples of these maps, including the galaxy 8715-3702 already shown in Fig. 1. For each source, we show the SDSS composite image, the [O III] flux density, the median velocity v_{med}, the multi-Gaussian-based W_{80} measurements, the single-Gaussian-based $W_{80,DAP}$, and the divisional values. We note that the number of spaxels with valid

values might differ between the $W_{80,DAP}$ map and the maps based on the here developed fitting routine. This is because we are only reporting measured quantities in pixels with an S/N of the [O III] emission line of >3 which might differ slightly from the DAP 'good' spaxels. Object 8715-3702 (Fig. 2) is classified as a Seyfert-AGN with high W_{80} measurements of ∼1000 km s^{-1} while the $W_{80,DAP}$ measurements are significantly lower. This difference is reflected in the 'division map' where the enhanced velocity line width in the north-west and east of the galaxy is apparent. Objects 8459-6102 (Fig. 3, classified as a regular SF galaxy) and 8978-9101 (Fig. 4, classified as LINER-AGN) both show a low gas velocity width and little difference between the W_{80} and $W_{80,DAP}$ measurements. That means that most fits are consistent with the single-Gaussian fit results suggesting that no or little enhanced gas kinematics are present in these sources.

4 RESULTS

4.1 Absolute kinematic comparison

We first perform an absolute kinematic comparison by assessing the distribution of W_{80} values in all MaNGA galaxies and in the AGN samples. Fig. 5 shows the distribution of all W_{80} measurements in every fitted spaxel of every MaNGA galaxy. We also separately show the distributions of the MaNGA-selected AGN and in non-AGN galaxies. The distribution peaks at ∼200 km s^{-1} which correspond to typical gas velocity widths in galaxies with masses of 10^{10-11} M$_{\odot}$. Additionally, we observe a heavily skewed tail towards large velocity widths, which is enhanced in MaNGA-selected AGN,
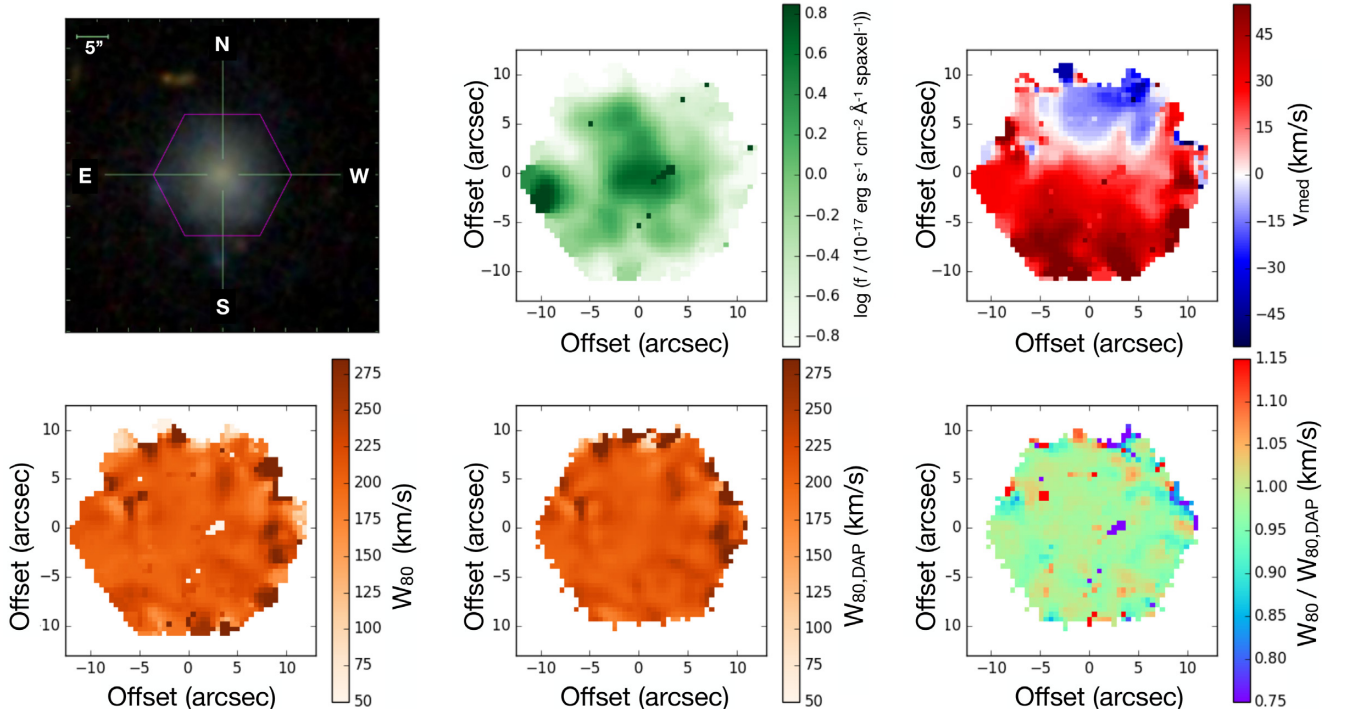
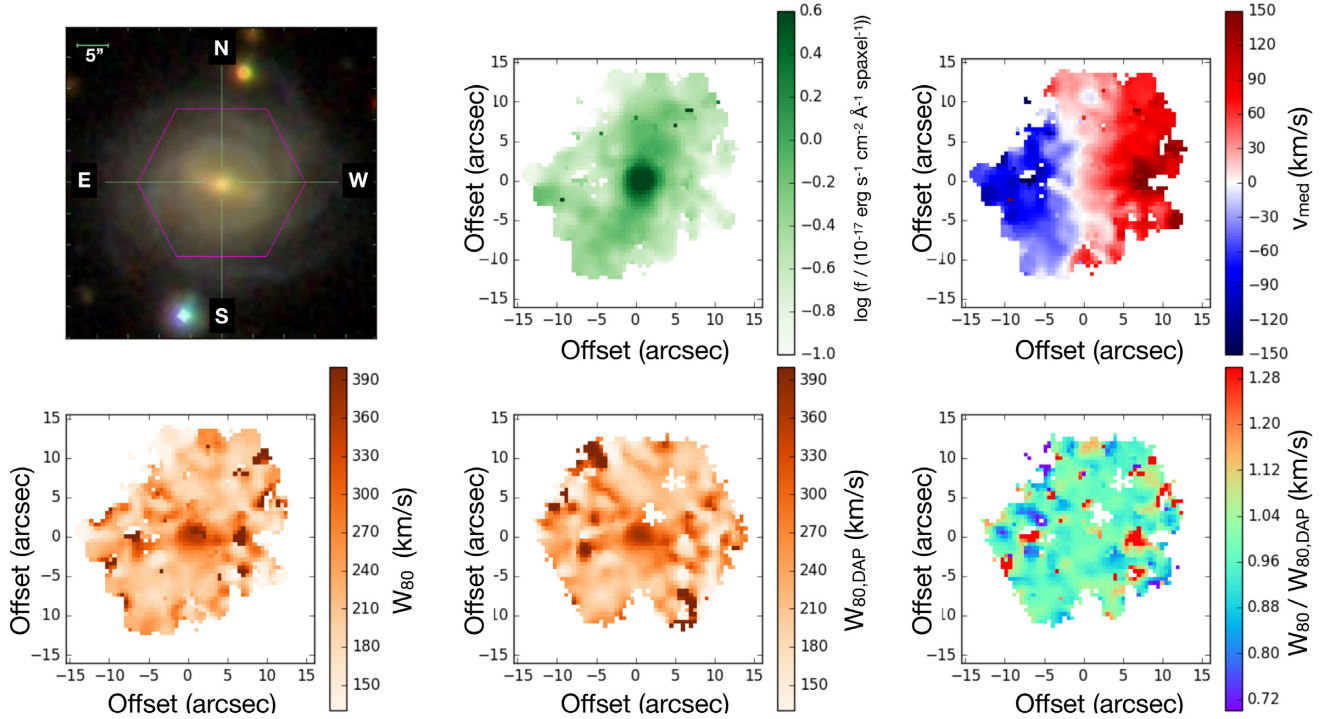**Figure 3.** Same as Fig. 2 but for MaNGA galaxy 8459-6102.

Figure 4. Same as Fig. 2 but for MaNGA galaxy 8978-9101.

indicative of kinematic peculiarities (Nelson 2000; Kewley et al. 2006).

In Fig. 6, we show the distribution of the mean W_{80} measurements $\langle W_{80} \rangle$ for all galaxies, for the MaNGA-selected AGN and the three different MaNGA-AGN subsamples, SF-AGN, LINER-AGN, and Seyfert-AGN. For this analysis, we only include galaxies in which at least 10 per cent of the spaxels have valid [O III] emission-line measurements, i.e. a peak S/N > 10. This cut was chosen to ensure that [O III] is detected in a significant enough number of spaxels and to be able make meaningful conclusions about the [O III] behaviour
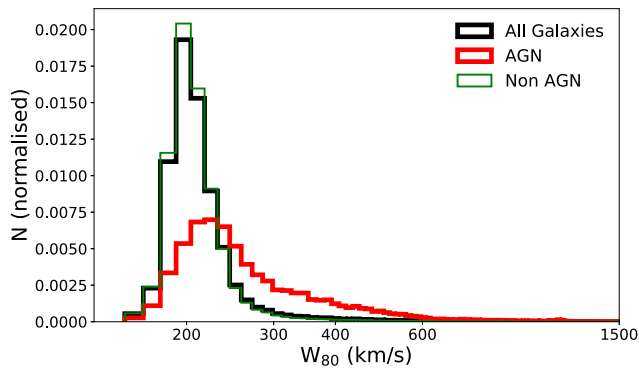
Figure 5. The distribution of W_{80} measurements across all spaxels in all 2778 MaNGA galaxies (black), the MaNGA-selected AGN (red), and non-AGN (green). The small number of values below 150 km s^{-1} are removed as they are at the limit of the instrumental resolution of the survey and not physically meaningful. Of particular interest is the largely skewed tail to values above 500 km s^{-1}, which is significantly enhanced for the MaNGA-selected AGN (p-value of KS-test $<10^{-200}$), indicative of enhanced kinematics potentially related to current or previous AGN activity.

in these galaxies. In total, 1116 MaNGA galaxies and 159 MaNGA-selected AGN fulfill this criterion.

For every galaxy, we furthermore measure the 75th percentile of their W_{80} distributions $W_{80, 75th}$. In Fig. 7, we show the distribution of the $W_{80, 75th}$ measurements for all galaxies, for the MaNGA-selected AGN and the three different MaNGA-AGN subsamples, SF-AGN, LINER-AGN, and Seyfert-AGN.

A two-sample Kolmogorov–Smirnov (KS) test shows that the $\langle W_{80} \rangle$ distributions of the MaNGA-selected AGN, the SF-AGN,

LINER-AGN, and Seyfert-AGN are significantly different from the total distribution. We repeat the analysis comparing the distribution of the MaNGA-selected AGN subsamples with only the non-AGN MaNGA galaxies and find similarly significant results. We report the measurements for $\langle W_{80} \rangle$ and $W_{80, 75th}$ in Table 1 and the p-statistic value of the KS-tests in Table 2. To investigate if these results are driven by any unaccounted bias, we randomly select 100 galaxies from the full sample and repeat the statistical comparison. A KS-test comparing the full and random galaxy sample results in a high p-value of $p = 0.47$ and shows that the W_{80} distribution of the randomly selected galaxy sample is drawn from the same distribution as the full MaNGA sample. We conclude that the statistical difference between the AGN and AGN-subsamples to the full MaNGA W_{80} distribution is indeed intrinsic and that the kinematic properties of the MaNGA-selected AGN is distinct from the overall MaNGA distribution.

To further illustrate this point, we compute the number of galaxies in which at least 10 per cent of the spaxels show W_{80} values of $W_{80} > 500/800/1000$ km s^{-1}. A total of 257/112/37 galaxies pass this cut. In the MaNGA-selected AGN sample, 77/21/7 (25/7/2 per cent) of the galaxies pass this cut while only 180/91/30 (7/4/1 per cent) of the remaining MaNGA galaxies do. Similarly, there are 13 MaNGA-selected AGN with $\langle W_{80} \rangle > 500$ km s^{-1} (4 per cent) and only 20 non-AGN with $\langle W_{80} \rangle > 500$ km s^{-1} (<1 per cent). The fractions were computed using the full MaNGA and MaNGA AGN sample as baseline, i.e. 2778 and 308 sources, respectively. Using the number of galaxies that initially passed our quality cut (at least 10 per cent of the spaxels need to have an [O III] line measurement with S/N > 10) as baseline, i.e. 1116 and 159 sources, respectively, leads to the same conclusion: two to three times as many MaNGA selected AGN show enhanced [O III] kinematics compared to the non-AGN in MaNGA.
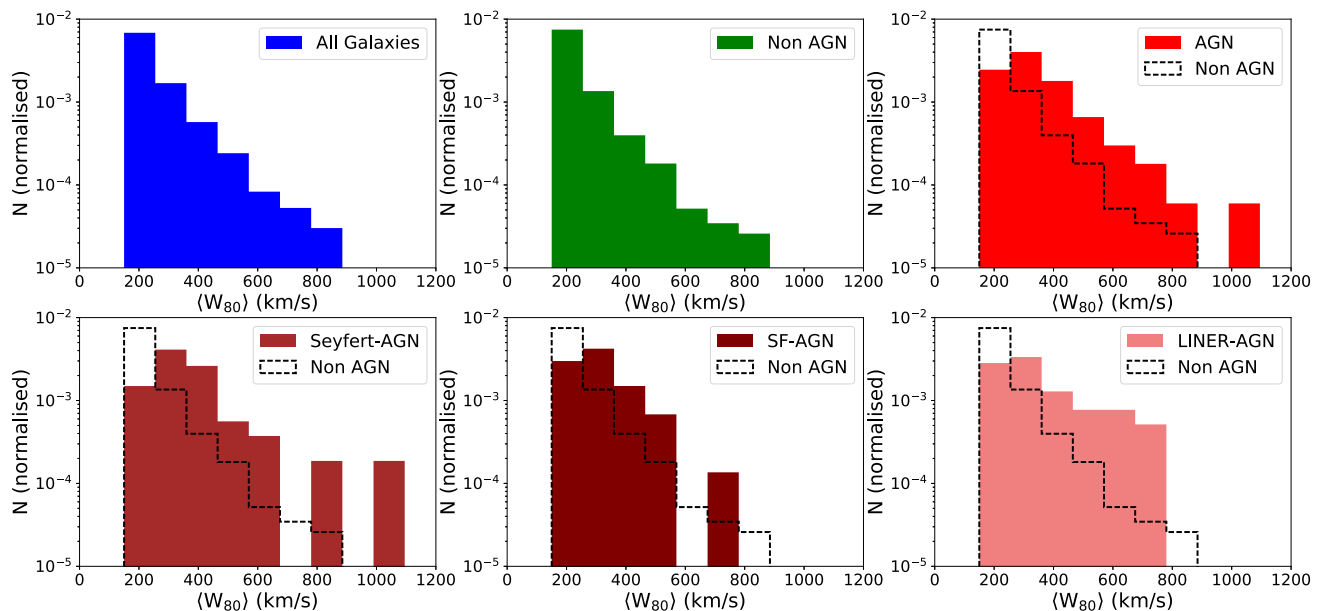

Figure 6. Normalized logarithmic distributions of the mean W_{80} measurements for each galaxy for the whole MaNGA sample, the MaNGA-selected AGN, the AGN subsamples, and the non-AGN. The small number of values below 150 km s^{-1} are removed as they are at the limit of the instrumental resolution of the survey and not physically meaningful. We show the distribution for all MaNGA galaxies (top left), non-AGN (top centre), AGN candidates (top right), and the AGN subsamples Seyfert-AGN (lower left), SF-AGN (lower centre), and LINER-AGN (lower right). For reference, we also show the non-AGN distribution (black dashed histogram) in the AGN and AGN subsample panels. In the AGN and all AGN subsamples, the distributions show larger contributions from high W_{80} measurements, indicative of enhanced kinematics potentially related to current or previous AGN activity.
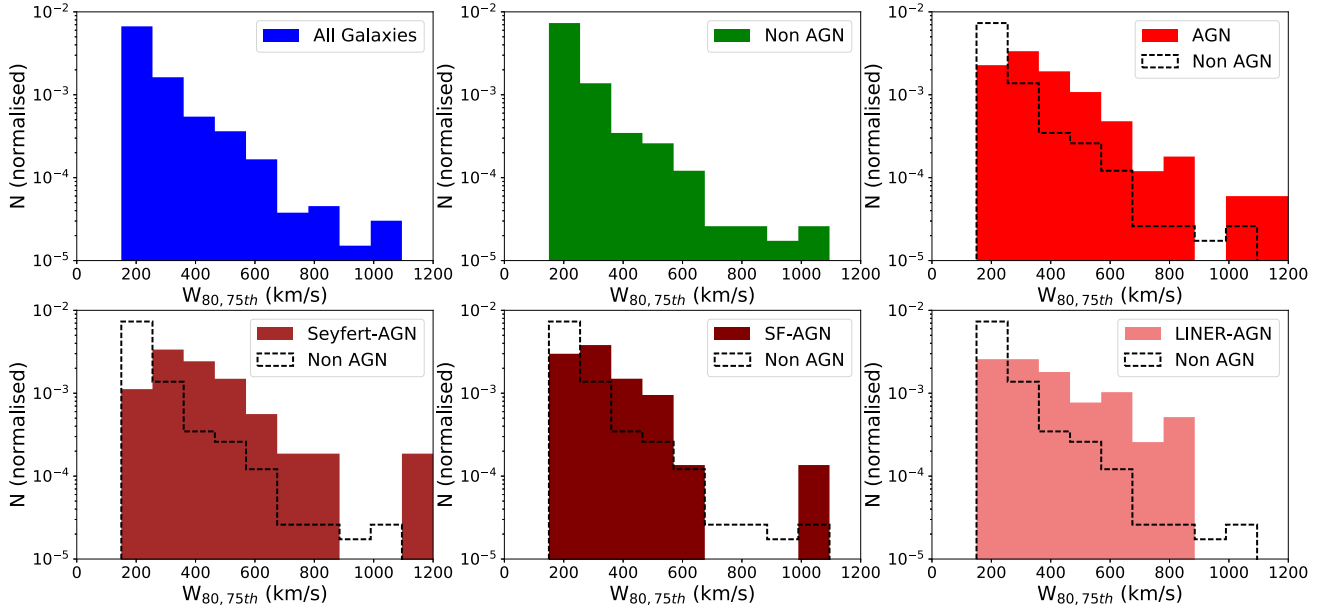
Figure 7. Normalized logarithmic distributions of the 75th percentile W_{80} measurements for each galaxy for the whole MaNGA sample, the MaNGA-selected AGN, the AGN subsamples, and the non-AGN. The small number of values below 150 $\mathrm{km\,s^{-1}}$ are removed as they are at the limit of the instrumental resolution of the survey and not physically meaningful. We show the distribution for all MaNGA galaxies (top left), non-AGN (top centre), AGN candidates (top right), and the AGN subsamples Seyfert-AGN (lower left), SF-AGN (lower centre), and LINER-AGN (lower right). For reference, we also show the non-AGN distribution (black dashed histogram) in the AGN and AGN subsample panels. In the AGN and all AGN subsamples, the distributions show larger contributions from high W_{80} measurements, indicative of enhanced kinematics potentially related to current or previous AGN activity.

Table 2. Results of the two-sided KS test comparing the distributions of the 'absolute kinematic comparison' shown in Figs 6 and 7 and the 'proportional kinematic comparison' shown in Fig. 8. We report the returned *p*-values when comparing the full MaNGA distribution and the non-AGN distribution to the AGN and AGN subsample distributions. Low *p*-values <0.01 show that the distributions are significantly different from one another.

	AGN	Seyfert-AGN	SF-AGN	LINER-AGN	Random
Absolute kinematic comparison (mean W_{80}):					
Full MaNGA	1.0e−23	3.4e−12	6.8e−10	4.7e−7	0.47
non-AGN	1.2e−31	2.4e−15	4.0e−13	1.5e−9	0.69
Absolute kinematic comparison (75th percentile W_{80}):					
	AGN	Seyfert-AGN	SF-AGN	LINER-AGN	Random
Full MaNGA	4.9e−23	1.3e−11	4.2e−12	1.7e−7	0.71
Non-AGN	9.8e−31	2.4e−14	9.5e−16	5.9e−10	0.98
Proportional kinematic comparison:					
	AGN				Random
Full MaNGA	1.5e−4				0.30
Non-AGN	5.9e−6				0.52

4.2 Proportional comparison

While the 'absolute kinematic comparison' presented above is sensitive to sources in which large values of W_{80} are observed, many outflow candidates and kinematically peculiar sources would not be selected. In low- and intermediate luminosity AGN driving outflows, the measured gas velocity widths are often of the order of the velocity widths expected of regular disc rotation (Greene & Ho 2005; Barbosa et al. 2009; Fischer et al. 2017; Wylezalek et al. 2017). In such sources, outflowing components can be better identified when broad, blueshifted components are present in the relevant emission lines, [O III] in our case. To quantify the

prevalence of such components, we analyse the difference between the velocity width maps provided by the MaNGA Data Analysis Pipeline (based on single Gaussian fits) and the velocity width maps derived in this work using the 'division maps' that report the fractional change between the pipeline velocity width and the here derived velocity width.

In order to quantitatively assess the differences between the single-Gaussian-based and multi-Gaussian-based velocity widths, we measure the fraction of spaxels in each galaxy for which the ratio between the single-Gaussian-based and multi-Gaussian-based velocity width exceeds a defined threshold. We define c as the
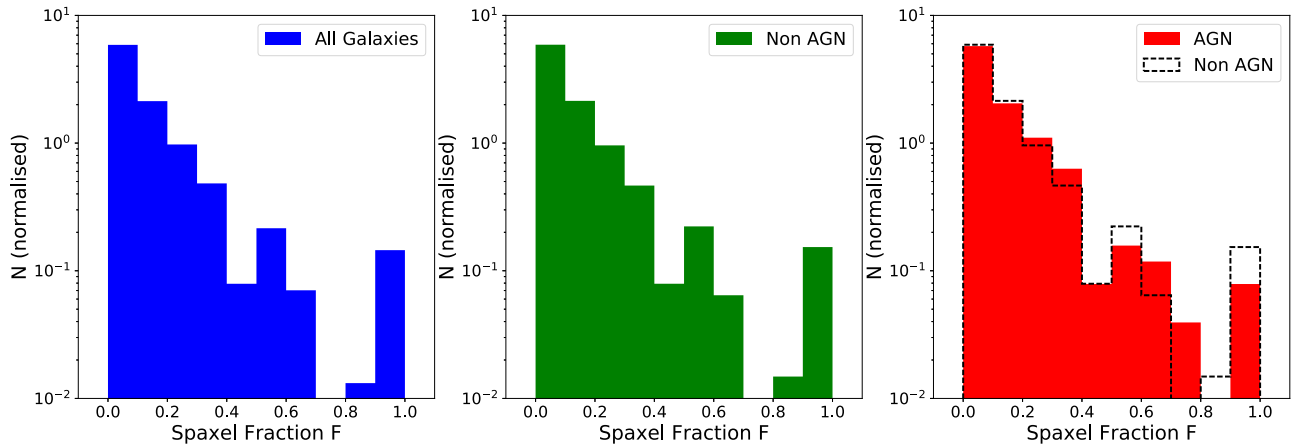
Figure 8. Distribution of spaxel fractions for which the ratio between the single-Gaussian-based and multi-Gaussian-based velocity width exceeds a defined threshold c. We show the normalized distributions for all MaNGA galaxies (left), non-AGN (centre), and MaNGA-selected AGN candidates (right) for a c value of 1.25.

threshold constant and show the distribution of spaxel fractions for $c = 1.25$ in Fig. 8. The figure shows the distribution of the fraction of spaxels F per galaxy with $W_{80} > 1.25 \cdot W_{80,\mathrm{DAP}}$. Due to low number statistics we here do not repeat the analysis for the different AGN subsamples. The results of the two-sided KS-test comparing the overall, non-AGN and AGN distributions to that of the full MaNGA sample are reported in Table 2. The KS-test shows very low p-values when comparing the AGN distribution to the full MaNGA and/or non-AGN distribution, showing that the kinematic properties in these sources are distinct. Visually inspecting the distributions, we note that indeed most of the differences between the AGN distribution and the overall MaNGA distribution lies in the high spaxel fraction tail. This shows that not only does the distribution of the AGN sample differ from the overall MaNGA distribution, but also that MaNGA-selected AGN show on average more spaxels where multiple Gaussian components were needed to describe the [O III] emission-line profile.

This trend is further quantitatively validated by introducing the following cut. We select galaxies where at least 25 per cent of the host galaxy's spaxels demonstrated at least a 25 per cent increase (this corresponds to $c = 1.25$) of their measured W_{80} values compared to $W_{80,\mathrm{DAP}}$. A 25 per cent increase is chosen to reflect areas of significant change, and 25 per cent of spaxels are required to limit the number of galaxies to a manageable amount while still identifying interesting sources. A total of 237 galaxies pass this cut out of 2778 total. 36 (11.6 per cent) of the galaxies in the AGN sample pass this cut compared to only 237 (9.5 per cent) of the remaining non-AGN.

To test for any potential biases in our analysis, we again draw a sample of 100 randomly selected galaxies from the overall MaNGA galaxy sample and repeat the analysis. A KS-test comparing the random distribution with the overall MaNGA distribution shows that the two distributions are statistically indistinguishable.

5 DISCUSSION

5.1 The prevalence of ionized outflow signatures in MaNGA galaxies

With the goal of assessing the prevalence of ionized outflow signatures in MaNGA galaxies and MaNGA-selected AGN, we

have shown that MaNGA-selected AGN candidates more frequently show enhanced [O III] emission-line kinematics than non-AGN in MaNGA. The difference in the gas kinematics between AGN and non-AGN galaxies is apparent in a variety of tests.

By measuring the velocity width of the [O III] emission line at 5007 Å W_{80}, we have first shown that the $\langle W_{80} \rangle$ and $W_{80,75\mathrm{th}}$ distributions of the full MaNGA sample are significantly different from the MaNGA-selected AGN sample and from the individual AGN subsamples. MaNGA-selected AGN candidates tend to have higher $\langle W_{80} \rangle$ and $W_{80,75\mathrm{th}}$ and two to three times as many MaNGA-selected AGN candidates show enhanced [O III] kinematics. In particular, we observe 2–3 times as many of AGN with a significant fraction of spaxels with $\langle W_{80} \rangle > 500$ km s^{-1} compared to the non-AGN sample. These gas velocity values are significantly higher than what is expected from regular disc rotation. The typical gas velocity dispersion of SDSS galaxies at $z < 0.15$ and $\log(M_*/M_\odot) < 11$ is $\lesssim 150$ km s^{-1} corresponding to W_{80} values of $\lesssim 380$ km s^{-1} (Thomas et al. 2013; Beifiori et al. 2014; Cicone, Maiolino & Marconi 2016; Übler et al. 2019). This suggests that a large fraction of the high velocity gas detected in the MaNGA-selected AGN is due to non-gravitational motions of the gas, potentially due to radiatively or mechanically AGN-driven outflows.

Most MaNGA-selected AGN are low-/intermediate-luminosity sources with $L_{[\mathrm{O\,III}]} \sim 10^{40}$ erg s^{-1} (Wylezalek et al. 2018). Since the [O III] luminosity can be used as an indicator of AGN bolometric luminosity if an AGN is present in the galaxy (Heckman et al. 2004; Reyes et al. 2008), this corresponds to a bolometric luminosity $L_{\mathrm{bol,\,AGN}} \sim 10^{43}$ erg s^{-1}. Recently, Fiore et al. (2017) have collected AGN wind observations for nearly 100 AGN and shown that the outflow velocity strongly depends on the AGN bolometric luminosity confirming previous studies. In many intermediate luminosity AGN, such as the AGN in this work, the velocities of any AGN-driven outflow therefore tend to be low ($v < 500$ km s^{-1}, Lena et al. 2015; Fischer et al. 2017; Wylezalek et al. 2017; Wylezalek & Morganti 2018) and single-Gaussian measurements and measuring the velocity width alone usually does not capture such low-velocity outflow activity. But additional kinematic components (such as outflows) often leave an imprint on the overall velocity profile of the relevant emission line ([O III] in our case) which can be identified by multi-component analysis of the emission lines. By identifying MaNGA galaxies in which the [O III] emission line is better described

by a two-component fit – compared to the single-component fit performed by the MaNGA Data Analysis Pipeline – we have shown that MaNGA-selected AGNs require more often a multicomponent model to describe their [O III] emission-line profiles suggesting an enhancement of broad secondary components being present.

The number of sources with outflow signatures identified in this paper is likely a lower limit. Since the analysis in this paper only captures sources with high [O III] velocity widths or [O III] velocity profiles with clear deviations from a Gaussian profile, weak and physically small outflow signatures below the spatial resolution of the MaNGA survey, such as the ones found in Wylezalek et al. (2017), would not be identified. A thorough modelling and subtraction of the gas velocity fields, which is beyond the scope of this paper, would be necessary to identify outflows through their residual signatures.

Our analysis shows that enhanced gas kinematics are clearly more prevalent in MaNGA-selected AGN than in non-AGN, but what are possible driving mechanisms? In low- and intermediate luminosity AGN, in which AGN-driven outflows are not expected to be of such high velocities that the AGN can be considered as the only possible driver, the effect of stellar feedback and merger-induced gas flows have to be considered as potentially contributing to the observed signatures.

To examine the contribution of star formation to the outflow activity, we show the relation between $\langle W_{80}\rangle$ and the star formation rate (SFR) in Fig. 10. Heckman et al. (2015) have shown that there is a strong correlation between the SFRs and the outflow velocities of starburst-driven winds which can be explained by a model of a population of clouds accelerated by the combined forces of gravity and the momentum flux from the starburst. While Heckman et al. (2015) measure the outflow velocity as the flux-weighted line centroid defined relative to the systemic velocity of the galaxy, a different definition (such as a W80 measurement) would not affect the qualitative sense of their results.

We cross-match the MaNGA catalogue with the MPA-JHU catalogue and use the SFRs reported there. The SFRs are derived using the 4000 Å break of SDSS single fibre spectra, following the method described in Brinchmann et al. (2004). We do not observe any significant positive correlations between SFR and $\langle W_{80}\rangle$ for either the total MaNGA distribution or only the AGN subsample. Especially for the sources with $\langle W_{80}\rangle > 500$ km s^{-1} the SFRs are not high enough to explain the observed high velocity widths. We also test whether there is any correlation between the specific SFRs and $\langle W_{80}\rangle$ and do not observe any.

We furthermore visually inspect all MaNGA-selected AGN with $\langle W_{80}\rangle > 500$ km s^{-1} and find the merger fraction to be ∼10 per cent. We find a similar fraction for the total MaNGA AGN candidate sample. In this analysis we have included all galaxies in close pairs, interacting galaxies and galaxies with visible merger signatures such as tidal tails. Rembold et al. (2017) find an even lower merger fraction in their AGN host galaxy sample of only a few per cent.

While we cannot fully exclude that starbursts and mergers contribute partially to the here observed enhanced [O III] kinematics, these results suggest that stellar-driven winds and merger-induced flows are not the dominant reason for why we observe high [O III] velocity widths in the MaNGA-selected AGN candidates with $\langle W_{80}\rangle > 500$ km s^{-1}. Furthermore, spatially resolved inflows in isolated galaxies are usually associated with low velocity dispersions of a few tens to 100 km s^{-1} (Storchi-Bergmann & Schnorr-Müller 2019), such that it seems unlikely that the high velocity dispersions observed here would be related to any inflows. The signatures are consistent with being due to radiatively or mechanically driven

AGN outflows. This type of analysis is more difficult for the AGN outflow candidates that show [O III] velocity profiles with clear deviations from a Gaussian profile (the ones identified in Section 4.2), but which do not necessarily have $\langle W_{80}\rangle > 500$ km s^{-1}. In the following section, we assess whether the kinematics of the additional kinematic components with which these profiles have been modelled agree with expectations from outflow models.

5.2 Inflow versus outflow?

Both types of comparisons presented in Sections 4.1 and 4.2 reveal that the [O III] kinematics of MaNGA-selected AGNs are different from the non-AGN in MaNGA. In the previous section, we have shown that the kinematics of the MaNGA AGN with $\langle W_{80}\rangle > 500$ km s^{-1} are consistent with being due to radiatively or mechanically driven AGN outflows. In AGN with an enhanced prevalence of secondary kinematic components but not necessarily high [O III] velocity widths, the kinematic signatures could be due to either outflows or inflows. In this section, we determine which scenario is more plausible.

We measure the velocity offset Δ between v_{DAP} and v_{med}, where v_{med} is the median velocity of the [O III] profile from our multi-Gaussian fit and v_{DAP} is the median velocity from the single-Gaussian DAP fit. For a pure Gaussian profile or a profile with an insignificant secondary component $v_{\mathrm{DAP}} \simeq v_{\mathrm{med}}$ and $\Delta v = 0$. In Fig. 9, we show the distribution of Δv values for all MaNGA spaxels that have a velocity width W_{80} greater than the mean W_{80} of their galaxy. This selection ensures that we only consider spaxels where the velocity width is indicative of out- or inflowing components. Fig. 9 shows that the distribution of Δv is slightly skewed towards negative Δv values when considering all MaNGA galaxies or only non-AGN in MaNGA. However, the distribution of Δv values for the MaNGA-selected AGN candidates is much more heavily skewed towards negative values. Although sometimes redshifted emission-line components have been associated with (AGN-driven) outflows (e.g. Müller-Sánchez et al. 2011; Fischer et al. 2013), because of dust attenuation blueshifted emission-line profiles are a better probe and signature of outflowing gas.

We cannot fully exclude that in some galaxies the enhanced prevalence of secondary kinematic components in the [O III] profile is not due to AGN-driven outflows, but rather due to signatures from mergers, bars or even inflows. But Fig. 9 shows that most secondary kinematic components in MaNGA-selected AGNs are blueshifted secondary components to the [O III] profile. This is an indication that we predominantly observe the signatures of outflows.

5.3 Non-AGN galaxies with outflow signatures

While we have shown that ∼2–3 as many MaNGA-selected AGNs show enhanced [O III] kinematics compared to MaNGA galaxies not selected as AGN, a significant number of MaNGA non-AGNs also show enhanced [O III] kinematics. We visually inspect the spatially resolved MaNGA-BPT maps and the corresponding maps of the Hα equivalent width (EW(Hα)) of all MaNGA non-AGN with $\langle W_{80}\rangle > 500$ km s^{-1}. All of those show BPT diagnostics consistent with AGN and/or LI(N)ER-like line ratios. However, they exhibit extremely low Hα equivalent widths with EW(Hα) <3 Å.

Cid Fernandes et al. (2010) have shown that invoking the Hα equivalent width allows to differentiate between the different ionization mechanisms that lead to the overlap in the LI(N)ER region of traditional diagnostic diagrams. Based on the bimodal distribution of EW(Hα), Cid Fernandes et al. (2010) suggest
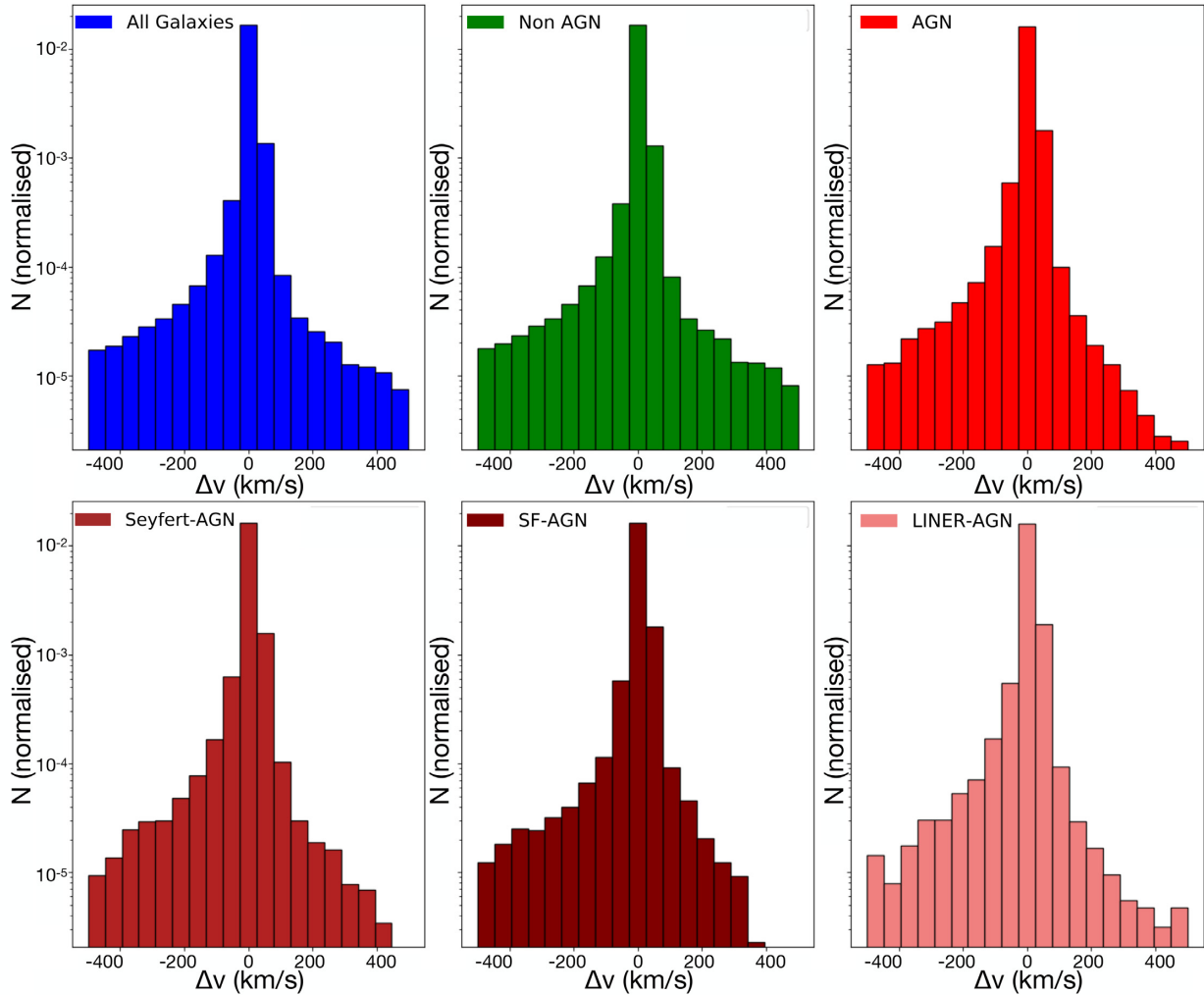
Figure 9. Distribution of the [O III] velocity offsets Δv, measuring the difference between the Gaussian-measured line-of-sight velocity and the non-parametric line-of-sight velocity as determined from our multi-Gaussian fitting and indicating whether the emission line is blueshifted or redshifted with respect to the Gaussian-measured line-of-sight velocity. We show the distributions for all galaxies in MaNGA (upper left), the non-AGN in MaNGA (upper centre), the MaNGA-selected AGN candidates (upper right), and the three AGN subsamples (lower row). The distribution of the MaNGA-selected AGN candidates and the three AGN subsamples are skewed towards negative Δv values, suggesting that we predominantly observe the signatures of outflows (rather than inflows) in these sources.

that EW(Hα) >3 Å optimally separates true AGNs from 'fake' AGNs in which LI(N)ER emission is due to hot evolved stars. As described in detail in Wylezalek et al. (2018), the MaNGA AGN selection takes this additional criterion into account which is why such sources have not been selected as AGN candidates. We observe now that in addition to the true AGN-selected candidates these 'fake' AGN make up the high velocity width tail from Fig. 6. This raises the question of what is driving these kinematic peculiarities.

Typical sources that have to be considered when observing [O III] velocity widths exceeding 500 km s^{-1} are mergers (Alaghband-Zadeh et al. 2012; Harrison et al. 2012) and outflows driven by stellar processes (Heckman et al. 2015). Alternatively, these sources may host AGN that have not been identified as AGN in the optical selection (Wylezalek et al. 2018) or relic AGN (Ishibashi & Fabian 2015) in which outflow signatures of a previous AGN episode are still imprinted on the gas kinematics. But a visual inspection of the optical images of these sources and the SFRs (see Fig. 10) does not suggest that mergers or stellar-

driven outflows are a major contributor to the observed kinematic peculiarities.

In Fig. 10, we furthermore mark objects that have been identified as 'passive radio sources' (Wylezalek et al. in preparation). These sources have infrared Vega colours, measured with the *Wide-field Infrared Survey Explorer (WISE)* satellite, of $-0.2 < W1 - W2 < 0.3$ and $0 < W2 - W3 < 2$, indicative of a passive galaxy population and no AGN activity (Stern et al. 2012). But these objects have high radio-to-IR flux ratios. This type of objects, potentially low-luminosity radio AGN, are sometimes associated with late feedback from AGN required to be strong enough to suppress the late cooling flows of hot gas and keep quiescent galaxies red and dead (Heckman & Best 2014). We now find that some of these objects make up the low SFR, high $\langle W_{80} \rangle$ tail in Fig. 10, suggesting that some of these identified high $\langle W_{80} \rangle$ sources are indeed active AGNs missed in the optical selection. In Wylezalek et al. (in preparation), we explore in detail the relation between the multiwavelength properties of AGN identified using various selection criteria and their gas kinematics.
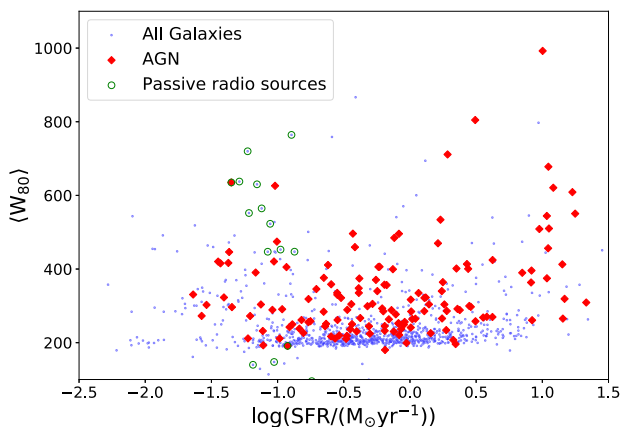
Figure 10. Relation between the mean W_{80} measurements $\langle W_{80} \rangle$ and the SFRs in all MaNGA galaxies (blue circles) and in the MaNGA-selected AGN (red diamonds). No significant correlation is observed in either sample suggesting that it is not stellar-driven winds that are the dominant reason for high $\langle W_{80} \rangle$ in both the all MaNGa sample and the MaNGA-selected AGN. Only sources that pass the quality cut described in Section 4.1 are plotted here.

5.4 AGN with no outflow signatures

It is also notable that many MaNGA-selected AGN candidates in this analysis do not show striking outflow signatures. Nedelchev, Sarzi & Kaviraj (2017) investigated nearly 10000 Seyfert galaxies selected from SDSS DR7 to look for cold-gas outflows traced by Na D, finding outflow signatures in only 0.5 per cent of the population compared to 0.8 per cent of the control galaxies. They conclude that nearby optical AGNs rarely drive kpc-scale cold-gas outflows and are not more frequent than in non-AGN. Similarly, Roberts-Borsani & Saintonge (2018) recently conducted a stacking analysis of the Na D doublet of 240 567 inactive galaxies and 67 753 AGN hosts from the SDSS DR7 survey to probe the prevalence and characteristics of cold galactic-scale flows local galaxies. They find little variation in either outflow or inflow detection rate between the AGN and non-AGN hosts. While this appears somewhat at odds with the findings in this paper, there are several plausible reasons for these different findings.

The first and most obvious one is that we may not be observing the same type of AGN and not the same type of outflows. As described in detail in Wylezalek et al. (2018), the AGN selection utilized in this paper is sensitive to a more nuanced picture of AGN activity and due to the IFU nature of the MaNGA survey, the selection allows to discover AGN signatures at large distances from the galaxy centre. In particular, the selection allows to identify AGN candidates which have been missed in the previous SDSS single fibre surveys. Additionally, the analysis in this paper focuses on ionized gas signatures whereas both studies cited above investigate the prevalence of neutral outflow/inflow signatures in local galaxies and AGN. While both simulations and observations show that AGN-driven outflows are multiphase phenomena, the actual link between the different gas phases participating in the outflow remains unknown (Guillard et al. 2012; Rupke & Veilleux 2013a; Costa, Sijacki & Haehnelt 2015; Santoro et al. 2018), especially because the AGN may ionize significant fractions of the neutral gas reservoir. Therefore, single-phase studies often lead to wrong or incomplete estimates of the prevalence, extent, mass, and energetics of outflows and may therefore lead to misinterpreting their relevance in galaxy evolution (Cicone et al. 2018).
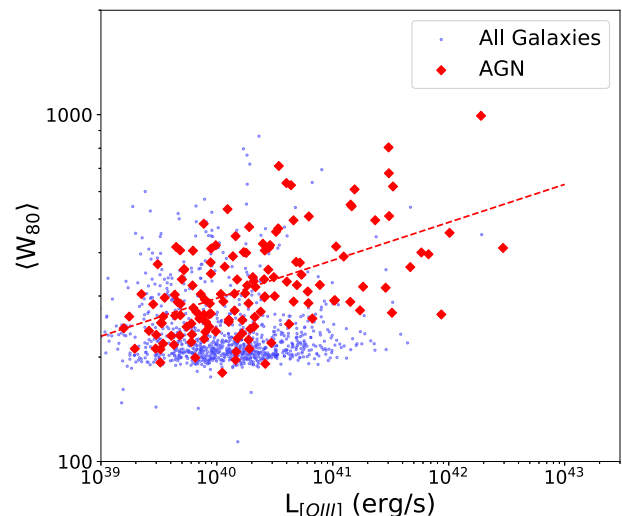

Figure 11. Relation between the mean W_{80} measurements $\langle W_{80} \rangle$ and the total [O III] luminosities $L_{\text{[O III]}}$ (an indicator for the bolometric AGN luminosity) in all MaNGA galaxies (blue circles) and in the MaNGA-selected AGN (red diamonds). We observe a significant positive correlation between $\langle W_{80} \rangle$ and $L_{\text{[O III]}}$ for the MaNGA-selected AGN suggesting that the AGN luminosity plays a dominant role in the launching and detection of winds. Only sources that pass the quality cut described in Section 4.1 are plotted here.

Na D absorption can, for example, be subject to significant uncertainties due to the fact that it can be probed only where there is enough background stellar light. Studying molecular outflows and their connection to ionized and neutral atomic phases in a sample of 45 local galaxies, Fluetsch et al. (2018) compute the ratio of the molecular to atomic neutral outflow rates $\dot{M}_{\text{H}_2}/\dot{M}_{\text{H I}}$. They use both the Na D absorption to compute neutral mass outflows rates and the fine-structure line of C+ , [C II] $\lambda157.74\,\mu$m, which is an alternative way to probe atomic neutral outflows. They find $\dot{M}_{\text{H}_2}/\dot{M}_{\text{H I}}$ to be an order of magnitude larger when using Na D absorption as tracer for $\dot{M}_{\text{H I}}$ compared to using [C II] as tracer for $\dot{M}_{\text{H I}}$. This comparison suggests that outflow detections and outflow mass measurements based on Na D absorption are likely lower limits and that a multiwavelength and multiphase assessment would lead to more complete and higher values/rates (Roberts-Borsani & Saintonge 2018).

In this work, we do find a significant difference between the prevalence of ionized outflow signatures in MaNGA-selected AGN compared to non-AGN with larger prevalence fractions than reported in the above cited works. For example, we find that 25/7/2 per cent of MaNGA-selected AGN candidates have $\langle W_{80} \rangle$ > 500/800/1000 km s^{-1} (see Section 4.1). However, the outflow prevalence fractions are still quite low. One of the reasons for this observation is certainly connected to the type of AGN we are probing, which are primarily weak AGN. Theoretical models (Zubovas & King 2012) suggest that AGNs need to provide sufficient luminosity to be able to push the gas out of the galactic potential. This 'threshold' nature of AGN feedback was recently also suggested by molecular gas (Veilleux et al. 2013) and radio observations (Zakamska & Greene 2014). Additionally, our observations are only sensitive to outflows on galaxy-wide scales. Small-scale outflows with the size of a few kpc would be missed in this analysis due to the limitations in spatial resolution (Wylezalek et al. 2017).

In Fig. 11, we show the relation between $\langle W_{80} \rangle$ and the total [O III] luminosity $L_{\text{[O III]}}$ as measured from the MaNGA observations.

Although $L_{[O III]}$ can be affected by extinction, most often from dust in the narrow-line region, [O III] luminosities are a good indicator of total bolometric AGN luminosity (Reyes et al. 2008; LaMassa et al. 2010). We observe a significant positive correlation between $\langle W_{80} \rangle$ and $L_{[O III]}$ for the MaNGA-selected AGN in this work. A Spearman rank test results in a p-value of 1.3×10^{-10}. We do not observe such a significant correlation for the whole MaNGA sample (p-value = 0.7). This result confirms previous observations that AGN luminosity plays a dominant role in the launching and detection of outflows (Zakamska & Greene 2014). Furthermore, Zubovas (2018) suggests that in galaxies with low gas fraction, typically low-redshift galaxies, AGNs are fed by intermittent gas reservoirs, and thus the typical AGN episode duration is short (for low-z AGN it is expected to be of the order of 10^5 yr, King & Nixon 2015; Schawinski et al. 2015a). Since such host galaxies are mostly devoid of gas, any outflow inflated by the AGN is difficult to detect because they are faint. With the MaNGA survey primarily targeting low redshift, low- and intermediate luminosity AGN, it is not unexpected that only a small fraction of MaNGA-selected AGNs selected exhibit clear and significant outflow signatures.

5.5 Spatial distribution of the [O III] velocity widths

We furthermore investigate the spatial distributions of the W_{80} measurements. As above, we limit our analysis to MaNGA galaxies in which at least 10 per cent of the spaxels have valid [O III] emission-line measurements, i.e. a peak S/N > 10. We then measure the mean W_{80} as a function of projected distance from the galaxies' centres in units of effective radii R_{eff}. By design, all MaNGA galaxies are covered by the MaNGA footprint out to at least 1.5 R_{eff}. In Fig. 12, we show the resulting radial profiles for the AGN and non-AGN samples, split by $\langle W_{80} \rangle$ and $L_{[O III]}$, respectively.

We observe a strong dependence of the AGN radial profiles on $L_{[O III]}$ where the AGNs with $L_{[O III]} > 2 \times 10^{40}$ erg s^{-1} exhibit a steep rise in W_{80} within the inner 0.4 R_{eff}, indicative of enhanced [O III] kinematics in the galaxy nuclei of luminous MaNGA AGN (Fig. 12, top panel). While the less luminous MaNGA AGN candidates do not show this steep rise in the centre, both the low and higher luminosity AGN samples show higher W_{80} measurements at all radii than the non-AGN samples. The non-AGN samples show mostly flat radial W_{80} profiles. We observe a tentative rise at $R < 0.4$ R_{eff} in the high luminosity non-AGN sample with $L_{[O III]} > 2 \times 10^{40}$ erg s^{-1}, showing that the non-AGN sample either includes AGNs that have been missed in the optical selection (see Section 5.2) and/or sources with strong nuclear starbursts driving enhanced [O III] kinematics.

Separating the AGN and non-AGN samples by their overall mean [O III] velocity width $\langle W_{80} \rangle$ (Fig. 12, bottom panel), we observe that the radial profiles of both the AGN and non-AGN samples with $\langle W_{80} \rangle > 500$ km s^{-1} are similar across all radii. Interestingly, neither of these profiles exhibits a significant rise towards the centre. Rather, both profiles are relatively flat out to $R = 1.5$ R_{eff}. Visually investigating the [O III] velocity width maps of these high $\langle W_{80} \rangle$ sources, we indeed confirm that the high velocity width signatures encompass the MaNGA footprint, indicative of large-scale enhanced [O III] kinematics, possibly related to galaxy-wide outflows. In these cases the radial extent of the outflows likely exceeds the probed 1.5 R_{eff} such that the outflow size probed here can only be regarded as a lower limit. These are not necessarily the most $L_{[O III]}$ luminous sources as the difference of radial profiles to the AGN and non-AGN samples with $L_{[O III]} > 2 \times 10^{40}$ erg s^{-1} shows. While we have shown in Fig. 11 that $L_{[O III]}$ generally correlates with $\langle W_{80} \rangle$, consistent with what has been found in other works (e.g.

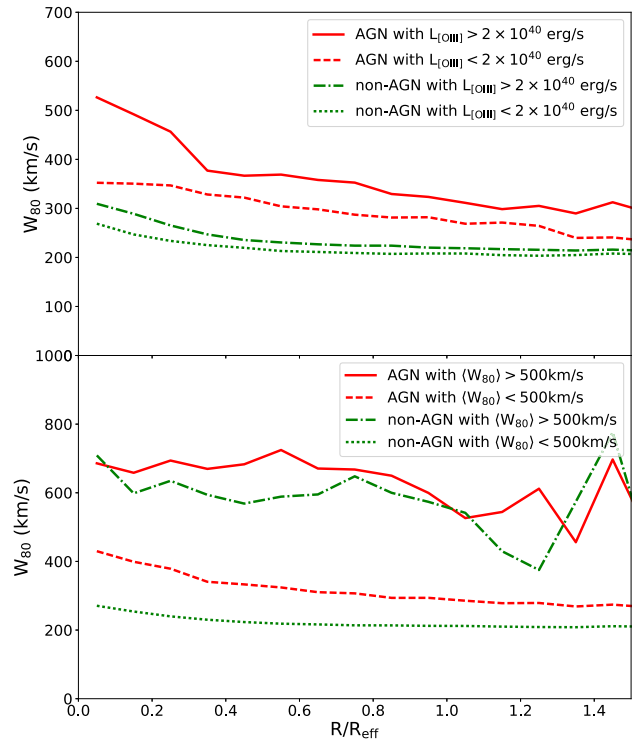**Figure 12.** Averaged radial dependence of W_{80} as a function of projected distance from the galaxies' centres in units of effective radii R_{eff}. *Top panel*: Averaged W_{80} radial profiles for the AGN and non-AGN samples, split by $L_{[O III]}$, respectively. *Bottom panel*: Averaged W_{80} radial profiles for the AGN and non-AGN samples, split by $\langle W_{80} \rangle$, respectively.

Zakamska & Greene 2014), there are some sources within both the AGN and non-AGN MaNGA samples with low- to intermediate [O III] luminosities that show evidence of large-scale disturbed [O III] kinematics. As discussed in Section 5.2 and shown in Fig. 10, the 'passive radio sources', possibly missed low-luminosity radio AGN, make up a large fraction of the high $\langle W_{80} \rangle$ population within the non-AGN sample.

The radial velocity width profiles of the AGN and non-AGN samples with $\langle W_{80} \rangle < 500$ km s^{-1} show significantly lower W_{80} measurements across all radii compared to the $\langle W_{80} \rangle > 500$ km s^{-1} samples. But the AGN sample with $\langle W_{80} \rangle < 500$ km s^{-1} consistently shows higher W_{80} measurements compared to the non-AGN sample with $\langle W_{80} \rangle < 500$ km s^{-1}, with a slight rise of the radial profile at $R < 0.4$ R_{eff}. This confirms our previous observations that the MaNGA-selected AGN in this work show distinct [O III] kinematics from the non-AGN sample with a higher prevalence of enhanced [O III] kinematics.

Several attempts have been made in the literature to quantify the size of AGN outflow regions and its relation to AGN power or galactic potential. However, this proves to be a difficult exercise as it is unclear what defines the 'size' of an outflow. For example, outflow sizes can be defined as the spatial extent of a region above a certain velocity width threshold (Sun, Greene & Zakamska 2017) or edges of outflowing bubbles (see Harrison et al. 2018, and references therein). Alternatively, outflow models assuming certain geometrical shapes of the outflowing region can be used to infer the maximum extent of the outflowing regions and deproject velocities. For example, Wylezalek et al. (2017) have used a bi-cone model described in Müller-Sánchez et al. (2011) which consists of two
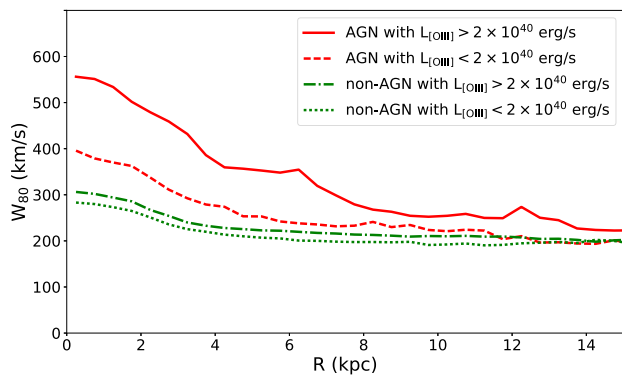
Figure 13. Averaged radial dependence of W_{80} as a function of projected distance from the galaxies' centres in units of kpc. We show the radial profiles for the AGN and non-AGN samples, split by $L_{[O\,III]}$, respectively.

symmetrical hollow cones having interior and exterior walls with apexes coincident with a central point source to model the outflow in an intermediate-luminosity MaNGA-selected AGN. However, this detailed modelling was only enabled by higher resolution follow-up IFU observations and is not available for all our source.

Here, we quantify the size of the outflow signatures in AGN in the following way. In Fig. 13, we show the averaged W_{80} radial profiles for the different $L_{[O\,III]}$ regimes as a function of absolute distance in kpc. Due to the different sizes of MaNGA galaxies, these radial profiles only provide a qualitative measurement of the difference in 'sizes' of the outflow region. We observe that in AGN with $L_{[O\,III]} < 2 \times 10^{40}$ erg s^{-1} the averaged radial profile reaches the level of the non-AGN at $\sim$8 kpc, whereas the radial profile of the AGN with $L_{[O\,III]} > 2 \times 10^{40}$ erg s^{-1} is starting to reach the level of the non-AGN samples at $\sim$15 kpc. We do not show the radial profiles as a function of distance in kpc for the low and high $\langle W_{80} \rangle$ populations (as we did in Fig. 12) due to the small sample size of the high $\langle W_{80} \rangle$ population leading to noisy radial profiles beyond 8 kpc.

The average [O III] luminosities $L_{[O\,III]}$ of the two AGN samples shown in Fig. 13 are 9×10^{39} and 2×10^{41} erg s^{-1}, respectively, while the average W_{80} measurements of the two AGN samples are 256 and 335 km s^{-1}, respectively. For an outflow with a velocity v_{gas} of these averaged W_{80} measurements, we can estimate the total kinetic energy injection rate over the lifetime τ of the ionized gas nebulae to be

$$\dot{E}_{kin} = \frac{E_{kin}}{\tau} = \frac{M_{gas} v_{gas}^2}{2\tau}, \tag{3}$$

where M_{gas} can be estimated from the [O III] luminosity under the 'Case B' assumption (Osterbrock & Ferland 2006; Nesvadba et al. 2011), assuming that [O III]/H$\beta \sim 10$ (Liu et al. 2013) and adopting an electron density $n_e = 100$ cm^{-3} (Greene et al. 2011). The gas mass can then be expressed as $M_{gas} = \left(\frac{L_{[O\,III]}}{10^{44} \, \text{erg s}^{-1}} \right) \cdot 2.82 \times 10^9$ M$_\odot$ (Liu et al. 2013). The lifetime τ of the episode of AGN wind activity may be estimated as the traveltime of clouds to reach the observed distances of 8/15 kpc from the centre travelling with the average outflow velocities v_{gas} quoted above. These calculations yields total kinetic energy injection rates of $\dot{E}_{kin} \sim 2 \times 10^{38}$ and $\sim 5 \times 10 \times 10^{39}$ erg s^{-1} for the low- and high-luminosity AGN samples, respectively. Although these calculations provide order-of-magnitude estimates at best, they show that (i) even in low/intermediate luminosity AGN, the positive correlation between AGN power and outflow energetics persist as expected from models

(Dempsey & Zakamska 2018) and seen in observations (Fiore et al. 2017, and references therein) but that (ii) the feedback processes in such low/intermediate luminosity, low-redshift AGN probed by MaNGA are unlikely to have a significant impact on the evolution of their host galaxies, i.e. fully suppress star formation processes, as the kinetic coupling efficiencies $\dot{E}_{kin}/L_{AGN}$ are $\ll 1$ per cent and most of them even likely $\ll 0.1$ per cent (see also Rodriguez del Pino et al. 2019). Although some theoretical models suggest that efficiencies as low as 0.5 per cent may be sufficient in substantially suppressing star formation in the host (e.g. Hopkins & Elvis 2010), most models require efficiencies of $\sim$5 per cent for feedback to be effective (see Harrison et al. 2018, and references therein). However, our calculations are based on ionized gas observations which only probe the fraction of the gas that is in the warm ionized gas phase. This gas is likely in dense clouds that remain largely optically thick to the AGN ionizing radiation and only a thin shell on the surface of these ionization-bounded clouds produces emission lines (Dempsey & Zakamska 2018). Therefore, there may be additional outflow components that are not captured by our calculations (Baron & Netzer 2019). Over the lifetime of the AGN (typically $\sim 10^7$ yr) and depending on the amount of cool gas present in the individual host galaxies, such continuous and ubiquitous energy injection and outflow activity may still heat a fraction of the cool gas and delay or suppress star formation in individual cases (Cheung et al. 2016).

5.6 Differences between AGN subsamples

In Section 4.1, we analysed the three different AGN subsamples introduced. We have shown that the distributions of the mean W_{80} measurements $\langle W_{80} \rangle$ of all three AGN subsamples are significantly different from the overall MaNGA distribution and the non-AGN distribution (see Fig. 6 and Table 2), with the AGN distributions being more skewed towards higher $\langle W_{80} \rangle$ measurements. The same observation is true when comparing the distributions of the 75th percentile W_{80} measurements $W_{80, 75th}$ (Fig. 7).

The Seyfert-AGN and SF-AGN are different from the full MaNGA and non-AGN distributions at a higher significance level (lower p-values) than the LINER-AGN distribution in both the $\langle W_{80} \rangle$ and the $W_{80, 75th}$ comparisons (Table 2). This observation, albeit tentative, might be explained by multiple factors. While the AGN selection method in Wylezalek et al. (2018) was developed such that 'fake' AGN with LINER-like signatures would not be selected as AGN candidates, the authors noted that some of the LINER-AGN may be sources where the LINER-like photoionization signatures are connected to AGN-unrelated shocks. If indeed some of the selected LINER-AGNs are related to shocks, while the shocks themselves may be due to AGN, stellar, or merger activity (see also Wylezalek et al. 2017), then one would expect that the LINER-AGN sample is not as 'clean' as the SF-AGN and Seyfert-AGN samples. Some of the LINER-AGN may in fact not be AGN. Therefore, LINER-AGN may show a lower rate of or different outflow signatures.

Generally, however, we observe little difference between the [O III] kinematics of the three AGN subsamples. In particular, the Seyfert-AGN and SF-AGN subsamples show very similar characteristics in their [O III] kinematics. The exact nature of the SF-AGN remains elusive. Various possibilities include recently turned off AGN, AGN dominated by a nuclear starburst, off-nuclear AGN, and these are currently still being investigated (Wylezalek et al. in preparation). Our kinematic analysis suggests that the rate and nature of weak outflows are similar in both subsamples.

6 CONCLUSION

In this work, we have examined the kinematics of the [O III] λ5007Å; emission line in each spatial element of 2778 low-redshift galaxies observed as part of the SDSS-IV MaNGA survey. Specifically, we have developed a customized fitting method that allows to account for potential secondary kinematic components in the emission-line profile as opposed to the MaNGA pipeline measurements that are based on single-Gaussian fitting. We first model the [O III] emission-line profile using both single and double-Gaussian profiles and evaluate the goodness of the fit based on its χ^2 value. We then utilize the non-parametric measurements W_{80} and v_{med} to quantify the width of the emission-line profile and the line-of-sight velocity. The main purpose of this work is to assess the prevalence of ionized gas outflow signatures in MaNGA-selected AGN candidates. Since MaNGA-observed AGNs tend to be low- to intermediate luminosity AGN, a careful analysis of faint broad secondary components and/or deviations from a simple Gaussian profile need to be carefully assessed.

Our strategy to do so is twofold. Only considering well detected emission lines with a signal-to-noise ratio S/N > 10, we first measure the mean $\langle W_{80} \rangle$ for each galaxy by averaging over all valid spaxels in that galaxy. We do not consider galaxies in which less than 10 per cent of the spaxels have valid [O III] emission-line measurements. We also determine the W_{80} value that marks the 75th percentile of each galaxy's W80 distribution $W_{80, 75th}$. Both $\langle W_{80} \rangle$ and $W_{80, 75th}$ indicated in an absolute fashion which galaxies show large velocity widths. This type of analysis may miss galaxies with slow/moderate outflows that are imprinted as small deviations from a pure Gaussian [O III] line profile. We therefore also assess the fractional change between the pipeline velocity width and the [O III] velocity width derived in this work.

Based on these derived quantities, we compare the [O III] kinematics in the full MaNGA sample to the non-AGN in MaNGA, the MaNGA-selected AGN candidates, and three subsamples of the MaNGA-selected AGN candidates. We find the following:

(i) The $\langle W_{80} \rangle$ and $W_{80, 75th}$ distributions of the full MaNGA sample are significantly different from the MaNGA-selected AGN sample and from the individual AGN subsamples where MaNGA-selected AGN candidates tend to show higher $\langle W_{80} \rangle$ and $W_{80, 75th}$.

(ii) Two to three times as many MaNGA-selected AGN candidates show enhanced [O III] kinematics. This result is based on determining how many galaxies/AGN show $W_{80} > 500/800/1000 \, \mathrm{km \, s^{-1}}$.

(iii) MaNGA-selected AGNs require more often a multicomponent model to describe their [O III] emission-line profiles compared to the non-AGN in MaNGA. While this result is more tentative, it suggests an enhancement of broad secondary components being present.

(iv) Comparing the line-of-sight velocities measured in this work to the line-of-sight velocities measured by the MaNGA pipeline, we find that the emission lines are predominantly blueshifted suggesting that the kinematic peculiarities observed in this work are indeed related to outflows (rather than inflows).

(v) While generally AGNs show a higher prevalence of ionized outflow signatures compared to the non-AGN in MaNGA, there are sources not selected as AGN that do show enhanced [O III] kinematics. These sources do not display an enhanced merger fraction or indications that stellar processes might be driving these outflow indicators. Such sources may host AGN or AGN relics that have not been identified by the optical selection methods used here. A thorough multiwavelength analysis is required to determine the cause of these enhanced [O III] kinematics.

(vi) We observe a significant correlation between the [O III] luminosity and $\langle W_{80} \rangle$ in the MaNGA-selected AGN, confirming similar measurements in other works using other AGN samples. Based on these results it seems that AGNs need to provide sufficient luminosity to be able to launch outflows and push the gas out of the galactic potential. Since most AGNs in MaNGA are of low-/intermediate luminosity, it is therefore no surprise that we detect outflow signatures in only ∼25 per cent of the MaNGA-selected AGN.

(vii) We find significant differences in the radial extent of broad [O III] velocity components between the MaNGA-selected AGN and non-AGN sources. Higher luminosity AGNs are able to drive larger scale outflows than lower luminosity AGN in agreement with in previous studies. The kinetic coupling efficiencies $\dot{E}_{kin}/L_{AGN}$ in MaNGA-selected AGN which are predominantly low- and intermediate luminosity sources are ≪1 per cent which might imply that these AGNs are unlikely to have a significant impact on the evolution of their host galaxies. However, these estimates are lower limits since we are likely missing a large fraction of the outflowing gas that is not in the here probed warm ionized gas phase. Over the lifetime of the AGN, continuous energy injection and outflow activity may still heat a fraction of the cool gas and delay or suppress star formation in individual cases even when the AGN is weak.

This work shows that ionized outflow signatures are more prevalent in MaNGA-selected AGN than in non-AGN. Much of this work has only been possible due to the added spatial dimension provided by the MaNGA IFU data and shows that outflow and feedback signatures in low-luminosity, low-redshift AGN may previously have been underestimated.

of Washington, University of Wisconsin, Vanderbilt University, and Yale University.

REFERENCES

Abolfathi B. et al., 2018, ApJS, 235, 42
Alaghband-Zadeh S. et al., 2012, MNRAS, 424, 2232
Baldwin J. A., Phillips M. M., Terlevich R., 1981, PASP, 93, 5
Barbosa F. K. B., Storchi-Bergmann T., Cid Fernandes R., Winge C., Schmitt H., 2009, MNRAS, 396, 2
Baron D., Netzer H., 2019, MNRAS, 486, 4290
Beifiori A. et al., 2014, ApJ, 789, 92
Blanton M. R. et al., 2017, AJ, 154, 28
Brinchmann J., Charlot S., White S. D. M., Tremonti C., Kauffmann G., Heckman T., Brinkmann J., 2004, MNRAS, 351, 1151
Bundy K. et al., 2015, ApJ, 798, 7
Cappellari M., 2017, MNRAS, 466, 798
Cappellari M., Emsellem E., 2004, PASP, 116, 138
Carniani S. et al., 2015, A&A, 580, A102
Cheung E. et al., 2016, Nature, 533, 504
Cicone C., Brusa M., Ramos Almeida C., Cresci G., Husemann B., Mainieri V., 2018, Nat. Astron., 2, 176
Cicone C., Maiolino R., Marconi A., 2016, A&A, 588, A41
Cid Fernandes R., Stasińska G., Schlickmann M. S., Mateus A., Vale Asari N., Schoenell W., Sodré L., 2010, MNRAS, 403, 1036
Comerford J. M. et al., 2020, ApJ
Costa T., Sijacki D., Haehnelt M. G., 2015, MNRAS, 448, L30
Crenshaw D. M., Fischer T. C., Kraemer S. B., Schmitt H. R., 2015, ApJ, 799, 83
Crenshaw D. M., Kraemer S. B., Schmitt H. R., Jaffé Y. L., Deo R. P., Collins N. R., Fischer T. C., 2010, AJ, 139, 871
Croton D. J. et al., 2006, MNRAS, 365, 11
Dempsey R., Zakamska N. L., 2018, MNRAS, 477, 4615
Drory N. et al., 2015, AJ, 149, 77
Fabian A. C., 2012, ARA&A, 50, 455
Ferrarese L., Merritt D., 2000, ApJ, 539, L9
Fiore F. et al., 2017, A&A, 601, A143
Fischer T. C., Crenshaw D. M., Kraemer S. B., Schmitt H. R., 2013, ApJS, 209, 1
Fischer T. C. et al., 2017, ApJ, 834, 30
Fluetsch A. et al., 2018, MNRAS, 483, 4586
Greene J. E., Ho L. C., 2005, ApJ, 627, 721
Greene J. E., Zakamska N. L., Ho L. C., Barth A. J., 2011, ApJ, 732, 9
Guillard P. et al., 2012, ApJ, 747, 95
Gunn J. E. et al., 2006, AJ, 131, 2332
Harrison C. M., Alexander D. M., Mullaney J. R., Swinbank A. M., 2014, MNRAS, 441, 3306
Harrison C. M., Costa T., Tadhunter C. N., Flütsch A., Kakkad D., Perna M., Vietri G., 2018, Nat. Astron., 2, 198
Harrison C. M. et al., 2012, MNRAS, 426, 1073
Heckman T. M., 1980, A&A, 87, 152
Heckman T. M., Alexandroff R. M., Borthakur S., Overzier R., Leitherer C., 2015, ApJ, 809, 147
Heckman T. M., Armus L., Miley G. K., 1990, ApJS, 74, 833
Heckman T. M., Best P. N., 2014, ARA&A, 52, 589
Heckman T. M., Kauffmann G., Brinchmann J., Charlot S., Tremonti C., White S. D. M., 2004, ApJ, 613, 109
Hopkins P. F., Elvis M., 2010, MNRAS, 401, 7
Ishibashi W., Fabian A. C., 2015, MNRAS, 451, 93
Johnson S. D., Chen H.-W., Mulchaey J. S., 2015, MNRAS, 452, 2553
Kauffmann G. et al., 2003, MNRAS, 346, 1055
Keel W. C. et al., 2017, ApJ, 835, 256
Kewley L. J., Groves B., Kauffmann G., Heckman T., 2006, MNRAS, 372, 961

King A., Nixon C., 2015, MNRAS, 453, L46
Kormendy J., Ho L. C., 2013, ARA&A, 51, 511
LaMassa S. M., Heckman T. M., Ptak A., Martins L., Wild V., Sonnentrucker P., 2010, ApJ, 720, 786
Law D. R. et al., 2015, AJ, 150, 19
Law D. R. et al., 2016, AJ, 152, 83
Lena D. et al., 2015, ApJ, 806, 84
Lintott C. J. et al., 2009, MNRAS, 399, 129
Liu G., Zakamska N. L., Greene J. E., Nesvadba N. P. H., Liu X., 2013, MNRAS, 436, 2576
Morton D. C., 1991, ApJS, 77, 119
Murray N., Chiang J., Grossman S. A., Voit G. M., 1995, ApJ, 451, 498
Müller-Sánchez F., Prieto M. A., Hicks E. K. S., Vives-Arias H., Davies R. I., Malkan M., Tacconi L. J., Genzel R., 2011, ApJ, 739, 69
Nedelchev B., Sarzi M., Kaviraj S., 2017, preprint (arXiv:1705.07994)
Nelson C. H., 2000, ApJ, 544, L91
Nesvadba N. P. H., Polletta M., Lehnert M. D., Bergeron J., De Breuck C., Lagache G., Omont A., 2011, MNRAS, 415, 2359
Osterbrock D. E., 1989, Astrophysics of Gaseous Nebulae and Active Galactic Nuclei. University Science Books
Osterbrock D. E., Ferland G. J., 2006, Astrophysics of Gaseous Nebulae and Active Galactic Nuclei. University Science Books, Sausalito, CA
Penny S. J. et al., 2017, MNRAS, 476, 979
Rembold S. B. et al., 2017, MNRAS, 472, 4382
Reyes R. et al., 2008, AJ, 136, 2373
Roberts-Borsani G. W., Saintonge A., 2018, MNRAS, 482, 4111
Rodriguez del Pino B., Arribas S., Piqueras Lopez J., Villar-Martin M., Colina L., 2019, MNRAS, 486, 344
Rudie G. C., Newman A. B., Murphy M. T., 2017, ApJ, 843, 98
Rupke D. S. N., Gültekin K., Veilleux S., 2017, ApJ, 850, 40
Rupke D. S. N., Veilleux S., 2011, ApJ, 729, L27
Rupke D. S. N., Veilleux S., 2013a, ApJ, 768, 75
Rupke D. S. N., Veilleux S., 2013b, ApJ, 775, L15
Sanchez S. F. et al., 2017, Rev. Mex. Astron. Astrofis., 54, 217
Santoro F., Rose M., Morganti R., Tadhunter C., Oosterloo T. A., Holt J., 2018, A&A, 617, A139
Sartori L. F. et al., 2016, MNRAS, 457, 3629
Schawinski K., Koss M., Berney S., Sartori L. F., 2015a, MNRAS, 451, 2517
Silk J., Rees M. J., 1998, A&A, 331, L1
Smee S. A. et al., 2013, AJ, 146, 32
Stern D. et al., 2012, ApJ, 753, 30
Storchi-Bergmann T., Schnorr-Müller A., 2019, Nat. Astron., 3, 48
Sun A.-L., Greene J. E., Zakamska N. L., 2017, ApJ, 835, 222
Sánchez S. F. et al., 2016, RMxAA, 52, 21
Thomas D. et al., 2013, MNRAS, 431, 1383
Übler H. et al., 2019, ApJ, 880, 48
Veilleux S., Cecil G., Bland-Hawthorn J., 2005, ARA&A, 43, 769
Veilleux S. et al., 2013, ApJ, 776, 27
Wake D. A. et al., 2017, AJ, 154, 86
Whittle M., 1985, MNRAS, 213, 1
Wylezalek D., Morganti R., 2018, Nat. Astron., 2, 181
Wylezalek D., Zakamska N. L., Greene J. E., Riffel R. A., Drory N., Andrews B. H., Merloni A., Thomas D., 2018, MNRAS, 474, 1499
Wylezalek D., Zakamska N. L., Liu G., Obied G., 2016, MNRAS, 457, 745
Wylezalek D. et al., 2017, MNRAS, 467, 2612
Yan R. et al., 2016a, AJ, 151, 8
Yan R. et al., 2016b, AJ, 152, 197
Yuan S., Strauss M., Zakamska N. L., 2016, MNRAS, 462, 1603
Zakamska N. L., Greene J. E., 2014, MNRAS, 442, 784
Zakamska N. L. et al., 2003, AJ, 126, 2125
Zubovas K., 2018, MNRAS, 473, 3525
Zubovas K., King A., 2012, ApJ, 745, L34

SUPPORTING INFORMATION

Supplementary data are available at *MNRAS* online.

Table 1. Mean and 75th percentile [O III] velocity width measurements $\langle W_{80} \rangle$ and $W_{80,\,75th}$ of all MaNGA galaxies analysed in this work.

Please note: Oxford University Press is not responsible for the content or functionality of any supporting materials supplied by the authors. Any queries (other than missing material) should be directed to the corresponding author for the article.

This paper has been typeset from a TeX/LaTeX file prepared by the author.